SANDIA REPORT
SAND2013-7915
Unlimited Release
October 2013

A Comprehensive Approach to Decipher Biological Computation to Achieve Next Generation High-performance Exascale Computing

Conrad D. James, Adrian B. Schiess, Jamie Howell, Michael J. Baca, L. Donald Partridge, Patrick Finnegan, Steven Wolfley, Daryl Dagel, Olga Spahn, Jason C. Harper, Kenneth Pohl, Seth Decker, Patrick Mickel, Andrew Lohn, Matthew Marinella

Prepared by
Sandia National Laboratories
Albuquerque, New Mexico 87185 and Livermore, California 94550

Sandia National Laboratories is a multi-program laboratory managed and operated by Sandia Corporation,
a wholly owned subsidiary of Lockheed Martin Corporation, for the U.S. Department of Energy's
National Nuclear Security Administration under contract DE-AC04-94AL85000.

Approved for public release; further dissemination unlimited.

Issued by Sandia National Laboratories, operated for the United States Department of Energy by Sandia Corporation.

NOTICE: This report was prepared as an account of work sponsored by an agency of the United States Government. Neither the United States Government, nor any agency thereof, nor any of their employees, nor any of their contractors, subcontractors, or their employees, make any warranty, express or implied, or assume any legal liability or responsibility for the accuracy, completeness, or usefulness of any information, apparatus, product, or process disclosed, or represent that its use would not infringe privately owned rights. Reference herein to any specific commercial product, process, or service by trade name, trademark, manufacturer, or otherwise, does not necessarily constitute or imply its endorsement, recommendation, or favoring by the United States Government, any agency thereof, or any of their contractors or subcontractors. The views and opinions expressed herein do not necessarily state or reflect those of the United States Government, any agency thereof, or any of their contractors.

Printed in the United States of America. This report has been reproduced directly from the best available copy.

Available to DOE and DOE contractors from
U.S. Department of Energy
Office of Scientific and Technical Information
P.O. Box 62
Oak Ridge, TN 37831

Telephone: (865) 576-8401
Facsimile: (865) 576-5728
E-Mail: reports@adonis.osti.gov
Online ordering: http://www.osti.gov/bridge

Available to the public from
U.S. Department of Commerce
National Technical Information Service
5285 Port Royal Rd.
Springfield, VA 22161

Telephone: (800) 553-6847
Facsimile: (703) 605-6900
E-Mail: orders@ntis.fedworld.gov
Online order: http://www.ntis.gov/help/ordermethods.asp?loc=7-4-0#online

SAND2013-7915
Unlimited Release
Printed October 2013

A Comprehensive Approach to Decipher Biological Computation to Achieve Next Generation High-performance Exascale Computing

Conrad D. James[1], Adrian B. Schiess[1], Jamie Howell[1], Michael J. Baca[1,2], L. Donald Partridge[2], Patrick Finnegan[1], Steven Wolfley[1], Daryl Dagel[1], Olga Spahn[1], Jason C. Harper[1], Kenneth Pohl[1], Patrick Mickel[1], Andrew Lohn[1], Matthew Marinella[1]

[1] Department Names
Sandia National Laboratories
P.O. Box 5800
Albuquerque, New Mexico 87185-MSXXXX

[2] University of New Mexico
MSC08 4740
1 University of New Mexico
Albuquerque, NM 87131-0001

Abstract

The human brain (volume=1200cm3) consumes 20W and is capable of performing > 10^16 operations/s. Current supercomputer technology has reached 1015 operations/s, yet it requires 1500m^3 and 3MW, giving the brain a 10^12 advantage in operations/s/W/cm^3. Thus, to reach exascale computation, two achievements are required: 1) improved understanding of computation in biological tissue, and 2) a paradigm shift towards neuromorphic computing where hardware circuits mimic properties of neural tissue. To address 1), we will interrogate corticostriatal networks in mouse brain tissue slices, specifically with regard to their frequency filtering capabilities as a function of input stimulus. To address 2), we will instantiate biological computing characteristics such as multi-bit storage into hardware devices with future computational and memory applications. Resistive memory devices will be modeled, designed, and fabricated in the MESA facility in consultation with our internal and external collaborators.

ACKNOWLEDGMENTS

We thank the Laboratory Directed Research and Development Office, and the Bioscience and Technology – New Directions (Cognitive Science and Technology) and Computing and Information Sciences Investment Areas for supporting this project. J. Christopher Forsythe (00431), John Wagner (1462), John Mitchiner (8004), Phil Bennett (1463), and Robert Leland (1000) were crucial in helping to steer this effort in the larger context of Sandia's national security missions. We thank the Microelectronics Development Laboratory staff and management at Sandia National Laboratories for device fabrication. We also extend our gratitude to Michael Rye and Bonnie McKenzie for focused ion beam serial sectioning and scanning electron microscopy. We also thank our Hewlett Packard collaborators Byung Joon Choi, J. Joshua Yang, Min-Xian Zhang, and R. Stanley Williams. We thank our University of Florida collaborators Sanal Buvaev, Andrei Kamalov, Hyoungjeen Jeen, Amlan Biswas, and Arthur F. Hebard. This work was funded under LDRD Project Number 151347 and Title "A Comprehensive Approach to Decipher Biological Computation to Achieve Next Generation High-performance Exascale Computing".

CONTENTS

1. Introduction 13
2. Dissociated cortical neuron characterization 17
    2.1. Optical stimulation of dissociated cortical neurons 17
        2.1.1. Primary neuron culture 18
        2.1.2. Optical stimulus instrumentation 19
        2.1.3. Data analysis 21
        2.1.4. Results 21
        2.1.5. Neuron Placement with Optical Tweezers 24
    2.2. Primary neurons in 3D hydrogel matrices 25
        2.2.1. Encapsulation of neurons in gels 25
3. Corticostriatal tissue network characterization 29
    3.1. Long-term depression in corticostriatal tissue networks 29
        3.1.1. LTD Methods 29
        3.1.2. LTD induction results 31
        3.1.3. LTD Discussion 32
4. Neuromorphic Microelectronic Device Design and fabrication 35
    4.1. History of neuromorphic and analog-like microelectronic devices 35
    4.2. Multiferroic devices for multi-bit memory storage 35
        4.2.1. Embedded microelectrode device structure 37
    4.3. Multilayered memristor devices with engineered conduction fronts 42
        4.3.1. Engineered conduction fronts in filamentary memristor devices 42
        4.3.2. Filament model in single and multilayered memristor devices 43
        4.3.3. Implications of multilayered memristor structures 46
    4.4. Design and fabrication of multilayered resistive memory devices 48
        4.4.1. Germanium selenide / silver resistive memory structures 48
        4.4.1. Multilayered resistive memory devices 49
    4.5. A physical model of switching dynamics in tantalum oxide memristive devices 49
        4.5.1. Filamentary memristor device structure and operation 50
        4.5.2. Phase change in the oxide material during switching 51
        4.5.3. On/Off switching as a function of pulse stimulus 54
        4.5.4. Linear and nonlinear contributions to switching dynamics 55
    4.6. Filament-based memristor device switching model and information storage 56
        4.6.1. Physics model of state switching in filamentary memristors 56
        4.6.2. Information storage in filamentary memristor devices 57
5. Neuromorphic circuit simulation and implementation – spice and xyce 59
    5.1. Example of a voltage to frequency converter with a memristor element 59
    5.2. Implementation of memristor model into Xyce 59
6. Conclusions 63
7. References 67

Distribution 102

FIGURES

Figure 1: Experimental setup for femtosecond laser stimulation and epifluorescence imaging of neurons. 71

Figure 2: Schematic of the optical setup for femtosecond laser stimulation and epifluorescence imaging of neurons. 72

Figure 3: Fluorescence response of neurons optically stimulated at 75mW average power (a-c) and at 160mW average power (d-f). (a) Brightfield image of a neural network showing the location of the focal spot (circle) and the cell body of interest (arrow). (b) Normalized intensity versus time calculated from the average fluorescence across the soma when exposed to 6 sets of optical irradiations (dashed lines). (c) Time derivative of the fluorescence showing the relatively intensity change between successive frames in the sequence. (d-f) Corresponding image and plots from a different sample at 160mW. 73

Figure 4: Differential fluorescence images of Ca^{2+} concentration after laser stimulation. The arrow denotes the laser stimulation location. 74

Figure 5: Variation of fluorescence response with laser pulse width. A linear fit to the data is also shown. 75

Figure 6: Red channel fluorescence over time for a solution with 20µM of propidium iodide (PI) added to the extracellular matrix. Several nearby cells in the field of view that were not directly stimulated are also shown. 76

Figure 7: Image of two neurons (arrows) placed into guidance cue nodes with laser tweezers on day 1 in culture. 77

Figure 8: (left) Sodium silicate derived matrix encapsulated 7 days. (right) Poly(glycerol) silicate derived matrix containing Neuro-basal medium (encapsulated 7 Days). 78

Figure 9: (top) Poly(glycerol) Silicate-derived matrix containing Neuro-basal medium and 1.5 mg/mL collagen (encapsulated 7 days). (bottom) Poly(glycerol) silicate derived matrix containing Neuro-basal medium and 2.5 mg/mL collagen (encapsulated 7 days). 79

Figure 10: A) Representative example of fEPSP population spikes before (gray) and after (red, blue) 4 x 10 Hz maximum HFS paradigm from STD cluster (> 70% recovery, n = 8, red) and LTD cluster (<60% recovery, n = 10, blue). B) Mean +/- SEM of individual LTD and STD clusters and combined data for test population spike amplitudes shown in C. C) Time course of normalized population spike amplitudes separated into 2 groups determined by cluster analysis of amplitudes during test period (30 min after HFS). 80

Figure 11: A) Percent recovery of population spike amplitudes before cluster analysis. Statistics: ANOVA multiple comparisons mean squares between groups = 7590.7, mean squares within groups = 1058.9, F = 7.1687, $p < 0.0001$with Scheffe's posthoc. B) Percent recovery of population spike amplitude for clusters with the weakest recovery. Statistics: ANOVA multiple comparisons, mean squares between groups = 5135.8 F=28.5296, $p < 0.0001$, with Scheffe's posthoc C) Percent recovery of population spike amplitude for clusters with the strongest recovery. Statistics: ANOVA multiple comparisons mean squares between groups = 883.3, F= 3.0877, $p = 0.016$, Scheffe's posthoc – no significant differences. 81

Figure 12: Clusters with 4 x 100 stimuli at max $I_{stim.}$ Percent recovery of population spike amplitude for all clusters with a HFS paradigm with 4 x 100 stimuli at maximum I_{stim}. Statistics:

ANOVA multiple comparisons, 2 × 3, mean squares between groups = 7790.4, F = 29.2047, $p < 0.0001$, with Scheffe's posthoc. 82

Figure 13: Effect of long-term plasticity on filtering for 10 Hz, 400 stimuli at maximum intensity HFS paradigm. A) Time course of normalized population spike amplitudes separated into 2 groups (STD and LTD). B) Low pass filter properties for 10 Hz, 400 stimuli at maximum intensity. 3^{rd} order Butterworth low pass filter fits to random frequency stimuli either before or after 10 Hz HFS paradigm. Clusters (RS# 1 (grey), COF = 4.3688 Hz, A=0.0185, n=22; RS# 2 STD cluster (red): COF = 14.2026 Hz, A = 0.0370; n = 7; RS# 2 LTD cluster (green): COF = 3.4474, A=0.0084; n=15). Inset shows averages of the lowest 3 frequencies used in random stimulus paradigm (n=6). C) Bar graph of STD (mean 92.50 +/- 4.87, red) and LTD (62.11 +/- 2.78, green) clusters of results 30 minutes after HFS from time course plots in A. D) Bar graph of ratio of 10 minute BL#1 to BL#2 for STD and LTD clusters. E) Comparison of RS# 1 (grey), RS# 2 STD cluster (red), and RS# 2 LTD cluster (green) frequency responses at 20.8 Hz, 35.2 Hz and 57.5 Hz. 83

Figure 14: (a) Surface interdigital microelectrode device configuration for a bismuth manganite ($BiMnO_3$, BMO) multiferroic thin film. Gold microelectrodes (Au) and the strontium titanate ($SrTiO_3$, STO) substrate are shown. Electric field lines (***E***) when voltage is applied across the microelectrodes and the subsequent induced bound charge out-of-plane polarization (P_{OP}) at the BMO/metal interface are also shown. (b) Embedded interdigital microelectrode device configuration for measuring in-plane ferroelectric properties. The in-plane (P_{IP}), out-of-plane (P_{OP}), and total vector polarization (P_{TOT}) are shown. (c) Degenerate ferroelectric polarization vectors corresponding to electric fields applied along the x and y axes of a ferroelectric film are shown. The total polarization vector (P_{TOT}) is also shown as a combination of the in-plane and out-of-plane polarization vectors. 84

Figure 15: a) Remanent ferroelectric polarization measured at 5 K via surface interdigital microelectrodes. Inset: AFM image of film morphology. b) Zero-field-cooled and field-cooled magnetization measured in a magnetic field of 1000 Oe is shown. Inset: magnetization vs. magnetic field hysteresis shows strong non-linearity and quasi saturation. 85

Figure 16:(a) Scanning electron microscope image of an embedded interdigital microelectrode array device. Bright-field image (inset). Scale bars = 10 μm. (b) Cross-sectional image of an embedded interdigital microelectrode array device (coated with two layers of Pt for milling/imaging). Scale bar = 200 nm. 86

Figure 17: (a) The out-of-plane (solid red line) and in-plane (dashed green line) remanent polarizations are shown for the surface and embedded interdigital electrodes, respectively, taken at 5 K. (b) The calculated total remanent polarization magnitude, P_{Tot}, inferred from P_{OP} and P_{IP}. 87

Figure 18: (a) Schematic of a conventional memristive device with an insulator layer sandwiched by a top (TE) and bottom electrode (BE). Conductive filaments made of mobile carriers grow under an electric field between the electrodes. (b) Simulation of the filament length distribution (n=100 filaments) in a single layer device. Filament lengths are sorted in ascending order for clarity. (c) A memristive device structure with multiple layers of alternating ionic mobility (μ_1, μ_2). (d) Simulation of the filament length distribution in the multi-layered device structure demonstrates larger average lengths with more uniformity than the distribution of the single layer device shown in panel b (dashed black line). 88

Figure 19: (a) Schematic of the phase-space coordinate layer-configuration (LC, see text), LC = 1.6 (bolded) was used for the switching profile shown in Fig. 2b. (b) The range of linear

resistance modulation is shown to be as much as 75% ΔR in the memristor structure with two ionic conductors (IC, red), a 75% increase compared to a conventional single ionic conductor memristor structure with ~ 44% ΔR (blue). The resistance curves are normalized by their OFF state resistances, which are calculated as: $R_{off}=(\sum \rho_n L_n)/A$ where ρ_n is the resistivity of each ionic conductor layer, L_n is the total thickness of all layers of that ionic conductor, and A is the area of the memristor structure. (c) Plot of the optimized design phase space for the increase in the range of linear resistive switching as a function of layer thickness and configuration. 89
Figure 20: (a) The capacitance switching of a conventional single layer memristor (1 IC, blue) and an alternating ionic conductor memristor (2 ICs, red) are compared. Inset: The device design for the capacitive switching behavior for Fig. 3a is shown. (b) The design space spanned by layer-thickness and layer-configuration is shown for capacitive switching, identifying optimal device design parameters. 90
Figure 21: The relative device-to-device (DTD) variability as a function of layer thickness and configuration. 91
Figure 22: Image of GeSeAg resistive memory devices fabricated in MESA 92
Figure 23: GeSeAg device operation. (left) Upon applying a positive voltage to the top electrode, silver drifts towards the bottom electrode and the device switches on (1-4). Upon applying a negative voltage to the top electrode, silver drifts back to the top electrode and the device switches off (5-6). (right) IV curve of a GeSeAg device with portions of the curve labeled according to the Ag motion shown on the left. 93
Figure 24: Schematic of a multilayer memristor stack using silver as the electrochemically-active electrode and platinum as the inert electrode. 94
Figure 25: IV switching curve for a single layer (TaOx) resistive memory device with a 20x20 μm^2 active area. 95
Figure 26: IV switching curve for a single layer (SiO_2) resistive memory device with a 100x100 μm^2 active area. 96
Figure 27: a) Memristor device structure, with the switching region magnified for clarity. b) A hysteretic IV curve from a tantalum oxide device with two stable resistance states ($R_{OFF}/R_{ON} > 10$). Inset: Triangular current waveform applied in IV hysteresis curves. c) Memristor resistance as a function of pulse number. Inset: The pulse/read waveform sequence used to modulate and measure the device state. 97
Figure 28:a) The low resistance state geometry of the switching region is shown. A Ta-rich core is surrounded by an oxygen concentration gradient (dashed line), transitioning from a sub-oxide region (TaO_x) to the Ta_2O_5 phase. The steady state filament radius, r_{SS}, is determined by the balance of flux due to the concentration gradient and temperature gradient (solid black line). The discontinuous outer edge contributes to non-linear conduction throughout r_{NL} and causes ruptures as r_F decreases. b) Geometry changes with an increase in resistance are shown: smaller steady-state radius, steeper temperature gradient, and an expansion of the Ta_2O_5 phase and contraction of the Ta filament by the amount dr_F. 98
Figure 29: a) Device resistance is shown as a function of applied voltage pulse number for ON switching, as calculated from the non-perturbative read measurement (V_{read} = 1mV). Each trace is the time-series of resistive switching for specific amplitudes of the 1 μs, state changing voltage pulse, with the arrow representing the direction of increasing amplitude (0.65 V to 1 V). Fits to Eq. 5 are shown in green. b) Equivalent data for OFF switching for voltages ranging from -1 V to -1.75 V. 99

Figure 30: IV curves measured at multiple resistance states spaced between R_{ON} and R_{OFF}. Fits according to the parallel conduction model of Eq. 6 are shown in green. Inset: Deviation from linear conduction showing the increasing contribution from parallel discontinuous non-linear conduction as the filament radius decreases. 100
Figure 31: (left) Schematic of a voltage to frequency converter circuit using a memristor active element. (right) Spice simulation of the memristor-based voltage to frequency converter....... 101

NOMENCLATURE

DOE	Department of Energy
SNL	Sandia National Laboratories
LTD	Long-term depression
STD	Short-term depression
HFS	High frequency stimulus
ANOVA	Analysis of variance
fEPSP	field excitatory post-synaptic potential
BMO	Bismuth manganite
PS	Population spike
VFC	Voltage to frequency converter

1. INTRODUCTION

This project addresses key issues in human decision-making and high-performance computing. On the first point, the mechanism by which massive amounts of data can be integrated, processed, and stored in the human brain remains a mystery. As an example, the cortex has a large number of neurons (10^{10}) and sends many inputs (prefrontal cortex, sensory, motor) to the striatum. A large amount of signal processing is performed in the corticostriatal networks that connect these two brain regions. Quantitative characterization of this information processing, including the ability to “reject” unwanted actions and to make decisions by integrating information to a threshold value [1], would improve our understanding of decision-making and enable the development of decision support tools and human factors methodologies.

These biological computing mechanisms are also of interest to high performance computing. As mentioned previously, biological networks maintain a significant lead over supercomputers in computations/s/W/cm^3. During the last several decades, neuromorphic computing strategies have emerged as a method to mimic the architecture of biological networks in silicon hardware [2]. However, these efforts have focused solely on mimicking neural tissue structure as opposed to mimicking neural tissue function. Thus, these circuits mimic the arrangement of neurons and neuron-neuron connections, but fail to mimic the molecular mechanisms and/or state-changes in neurons by which actual computation occurs in neural tissue. For instance, synaptic connections between biological neurons are thought to be the basic unit of computation, yet many early efforts in neuromorphic computing focused on hardware CMOS transistor “neurons” connected by software “synapses.” Other efforts have involved the fabrication of large multi-transistor hardware “synapses” that are 10^3 too large to be scaled to biological synapse densities (10^{10} connections/cm^2). However recent work has demonstrated the potential of mimicking molecular mechanisms in neurons. Newly discovered memristor structures are capable of storing information, and these components scale in sizes similar to that of biological synapses [3]. Jo et al. demonstrated spike-timing-dependent plasticity (STDP) in memristor structures [4], a phenomenon observed decades ago in biological synapses in which a synapse connection grows stronger when the pre-synaptic neuron fires before the post-synaptic neuron. Arrays of memristors were recently combined with CMOS to create logic devices [5], yet despite these advances, substantial challenges remain to utilize these technologies in conventional electronics and next-generation supercomputers.

This project addresses these challenges with the following tasks: 1) characterize the frequency-dependence of plasticity in biological corticostriatal networks and 2) design, fabricate, and characterize neuromorphic memory/computation hardware devices.

2. DISSOCIATED CORTICAL NEURON CHARACTERIZATION

Our previous work in engineered neural tissue networks [6] developed tools for constructing and interrogating in vitro neural networks. In vitro preparations of neurons present significant challenges to stimulation/recording studies given the difficulty in 1) providing directed stimulation to specific neurons and 2) tracking which neurons respond to the stimulated cell. In order to assess the information processing in these types of networks, we needed to use a method that would allow directed stimulation of particular sites in a network while also tracking the response of multiple nearest neighbor cells. We thus focused on optical stimulation and monitoring of activity in dissociated neurons. This work is currently being prepared for submission to a journal for publication.

2.1. Optical stimulation of dissociated cortical neurons

Near-infrared (NIR) ultrashort pulsed laser irradiation has been used in biology and the life sciences for a wide range of applications, from advanced imaging and spectroscopy, to cell manipulation and fusion, to nano-surgery and transfection [7-9]. The usefulness of NIR pulsed lasers derives from their nonlinear (multiphoton) absorption at focus that results in high peak power yet low mean energy as well as the long penetration depth and low scattering in biological samples. In neuroscience, NIR femtosecond lasers have been utilized as a noncontact, noninvasive alternative (or complement) to electrical stimulation of neurons and astrocytes [10-12]. Combined with fluorescence calcium imaging, this approach to neural stimulation has been applied to the study of neural activity, connectivity, and function [11, 13, 14].

Previous studies of femtosecond stimulation of neurons [10-20] have proposed essentially two mechanisms induced by the laser: photo-disruption and photo-poration, where the transition from a dominant disruption mechanism to a dominant poration mechanism occurs at laser power densities ~ 5×10^{11} W/cm^2 (e.g. ~35mW of 800nm, 100fs, 80MHz light focused with a 0.9 NA objective). These studies are consistent with the in-depth analysis of Vogel et al. [7], where the transition from transfection to cell damage occurs near this irradiance level. The photo-disruption mechanism proposed thus far involves a laser-induced release of calcium ions (Ca^{2+}) from the intracellular calcium stores in the cytoplasm that triggers a massive release of Ca^{2+} into the cytosol, and a subsequent rise in fluorescence as it binds to the dye molecules. Nothing similar has been proposed for stimulation outside of the soma, although calcium stores exist in the neural processes as well. In photo-poration, the focused laser spot generates sufficient free electrons through ionization to form a low density plasma at the membrane surface that opens a small, transient pore, which allows entry of extracellular calcium [18]. This stimulation mechanism can occur anywhere in the cell, including the axon and dendrites.

In this study, a NIR femtosecond laser was used to stimulate cultured, cortical neurons and to record the resulting activity from the enhanced Ca^{2+} fluorescence. An irreversible and delayed response is observed that is highly dependent on the influx of extracellular Ca^{2+} primarily through the native membrane channels rather than from a laser-induced poration. A second, fast activity (~sec.) was also observed that is triggered by the fluorescence light source. This spontaneous activity is stochastic and reversible and independent of the laser stimulation.

2.1.1. Primary neuron culture

Cortical tissues dissected from the brains of embryonic day 18 Sprague-Dawley rats were obtained from Genlantis (San Diego, CA). Tissue dissociation and culture were performed the day of arrival following the manufacturer's suggested protocol. Briefly, tissue was allowed to settle for 15 minutes at 4°C and shipping medium was removed for later use. NeuroPapain™ enzyme (Genlantis) dissolved in NeuroPrep™ medium (Genlantis) at a concentration of 2 mg/mL was added to the tissue (2 mL final volume) and incubated at 30˚C for 30 minutes with gentle agitation every 2 minutes to digest tissue and aid in cell dissociation. After incubation, the suspension was allowed to settle and the supernatant removed. One mL of shipping medium was added back to the tissue, and gentle trituration with a 1 mL pipet tip was performed until most of the cells were dispersed in solution. The cell suspension was added to the remaining volume of shipping medium and the dissociated cells pelleted at 400 x *g* for 4 minutes. The supernatant was removed and the cell pellet resuspended in 1 mL Neurobasal Medium™ (Invitrogen, Carlsbad, CA) supplemented with 0.5 mM Glutamax™-I (Invitrogen) and 1X serum-free B27® (Invitrogen). A 2 µL aliquot of cells was mixed with 18 µL of 0.4% Trypan Blue (Sigma-Aldrich, St. Louis, MO) and dye excluding cells counted using a hemacytometer. Cells were further diluted to a concentration of 10^6 cells/mL and plated at a density of 18 x 10^3 cells/cm^2 onto prepared substrates. Cells were incubated for 1 hour at 37˚C, 5% CO2 with 10 µg/mL Gentamycin Reagent Solution (MP Biomedicals, LLC, Solon, Ohio), after which, the medium was replaced with fresh, pre-warmed medium. Every three to four days, a 50% medium change was performed and the cells were inspected for growth.

At specified intervals, healthy cultures were fixed for subsequent staining and imaging. Cell media was removed from the substrate and immediately replaced with a small volume of 2% Paraformaldehyde (Electron Microscopy Sciences, Hatfield, PA), 4% D-Sucrose (Fisher Scientific, Pittsburgh, PA) solution in 1X PBS (Mediatech, Manassas, VA). Cells were fixed for 30 minutes, after which, the substrates were rinsed once with 1X PBS solution and stored in 1X PBS at 4°C prior to staining. Samples were permeabilized to allow antibodies to penetrate the cells with a permeabilization solution for at least 10 minutes. Following this they were washed 3 times with PBS. Next, they were blocked with a BSA solution for 1 hour at 37C, followed by incubation in antibody dilution buffer, and 3 rinses with PBS. Next, they were incubated with a primary antibody(s) for 1 hour at room temperature, followed by 3 rinses in antibody dilution buffer. Next, they were incubated with secondary antibody(s) if necessary for 1 hour at room temperature, followed by 3 rinses in antibody dilution buffer. In some cases primary antibodies were conjugated with secondary fluorescent antibodies so secondary antibody incubation was not necessary. Finally in cases where a nuclear DAPI stain was used, it was incubated for 5 minutes, followed by two rinses in PBS. The samples were kept in the last PBS rinse prior to imaging. All incubation steps involving fluorescent antibodies as well as storage prior to imagine were done using minimal light (turned off main lighting, use of aluminum foil covering) to minimize the potential for bleaching. Antibodies/fluorophores used include tau1 (Alexa 594), MAP2 (Dylight 488), and a BODIPY dye that binds to DNA to highlight cell nuclei.

2.1.2. *Optical stimulus instrumentation*

The oscillator output (1030nm, 200fs, 30MHz) of a diode-pumped Ytterbium femtosecond laser (HP s-Pulse, Amplitude Systemes, France) was coupled into an inverted, fluorescence microscope (Eclipse Ti-E, Nikon Instruments, Melville, NY) equipped with an infinity-corrected objective (20×, NA=0.45, air immersion) and a laser dichroic and FITC filter set (Semrock, Rochester, NY). The stimulation period was controlled by a mechanical shutter (Uniblitz, Rochester, NY), and the average sample power was 75mW.

Fluorescence measurements were taken with an inverted microscope (Eclipse Ti-E, Nikon Instruments, Melville, NY) equipped with a low-noise CCD camera (Clara, Andor

Technology, Northern Ireland) and a 20× infinity-corrected objective (S Plan Apo ELWD 0.45, Nikon Instruments), as shown in Figure 1. Neural stimulation was accomplished using the oscillator output (1030nm, 200fs, 30MHz) of an Ytterbium femtosecond laser (HP s-Pulse, Amplitude Systemes, France). Laser exposure was controlled by a mechanical shutter (Uniblitz, Rochester, NY), while average power was regulated by a ½-wave plate and a Glan-laser polarizer (Thorlabs GmbH). An optional zero-order, ¼-wave was used to circularly polarize the stimulation light. Two successive beam diameter adjustments, a 10× expansion followed by a 2× reduction (Thorlabs), were implemented to match the back-aperture of the objective and to ensure that the laser focal plane coincides with the brightfield image plane. The final element in the stimulation path, a laser dichroic beamsplitter (Semrock, Rochester, NY), reflected the laser wavelength (~94%) yet transmitted the visible fluorescence (~96-97%) to the imaging path.

Potentially healthy and dead cells were screened with the baseline fluorescence excited by a mercury broadband source (Intensilight, Nikon Instruments) coupled with fluorescein isothiocyanate (FITC) and ethidium homodimer (EthD-1) cubes (Semrock), respectively. A second mechanical shutter (Uniblitz) matched the on-time of the excitation light to the camera exposure, thereby limiting photobleaching effects. Both the laser and broadband shutters were triggered by a programmable pulse stimulator (Master-8, A.M.P.I., Israel) linked to the internal signal from the control software (NIS Elements, Nikon).

The canonical stimulation paradigm consisted of 100ms bursts of 200fs infrared light at 75mW average power. At 30MHz repetition rate, this means that over 3 million pulses with energy of 2.5nJ and peak power of 12.5kW are applied with each burst. By 160mW average power, cell blebbing and visible damage (boiling, lysing) were evident. Lower repetition rates (1, 10, 100kHz) were also experimented with using the amplified output beam of the laser (500fs pulse width). For these rates, the average power was adjusted to produce ~10nJ/pulse at the sample.

For optical stimulation studies, we used neurons 10-14 days old loaded with Fluo-4-AM dye. The density of neurons in the camera field-of-view (450 × 335 μm^2) ranged from 2-23 cells, the average being 7 cells. Candidate cells for optical stimulation were selected first for their healthy physical appearance under brightfield illumination, second for their relative dimness in the FITC channel (i.e. not saturated—not completely loaded with Fluo-4 dye), and finally for their darkness in the EthD-1 channel, which enters the nuclei of dead cells. The focal spot of the laser was positioned either over the soma itself or along the main process radiating out from the soma, presumably the axon. The cell threshold response to laser activity occurred at ~60mW. Even at this threshold level, the effect is cumulative and non-reversible and tends toward saturation, counteracted by photobleaching and expulsion of calcium-bound dye molecules. This was true even before laser stimulation, as the brightest cells were essentially saturated and therefore not responsive to the laser, and only the dimmer cells showed measurable laser activity.

2.1.3. Data analysis

Fluorescence sequences were analyzed by a custom Matlab® program. In brief, individual cells are extracted from the background by a combination of binary thresholding, morphological operations, and watershed segmentation using the FITC fluorescence image either before or after laser stimulation. Initially, the entire image is processed for potential cells, but only those manually selected by the user are analyzed. In addition to providing maximum flexibility, this manual selection step also makes distinguishing between overlapping cells much easier. Based on the relative intensity and size of the internal morphology of the cells, a further refinement of the cell segmentation is also included to remove the nuclear region from the analysis. The output of the segmentation is a binary mask, for which the average intensity within each region is logged at every time step in the sequence. Individual neuron processes were analyzed in a similar way, except segmentation was accomplished by the NeuronJ plugin for ImageJ.

2.1.4. Results

Figure 3 shows a typical fluorescence response of cells stimulated multiple times in 100ms bursts at 75mW and 160mW average laser power. In both cases (b & e), the soma fluorescence increased significantly during the second set of pulses (60-69s) and saturated by the end of the third set at 75mW and at the end of the second set at 160mW. No further increase of fluorescence is seen during the pulse trains 3-6 for the 160mW case, whereas diminishing responses are evident at 75mW for these pulse trains. This is especially evident from (c) and (f), which show the coincidence of the laser stimulation and the calcium flux as the (positive) time derivative from frame to frame. As shown, the timescale for the expulsion and photobleaching of the calcium-bound dye molecules is on the order of several minutes.

The dynamics of the calcium flux can be seen in Figure 4, which shows 8 difference images (I_{i+1} - I_i) in a 5min. sequence for cells stimulated with 75mW. Extracellular Ca^{2+} influx first occurred at the laser focus (indicated by the arrow) and then moved outward along the neuronal processes. At 42s, the neuron to the right of the stimulation point fluoresces strongly, including its distal processes. This neuron repeatedly cycles over the next 20s before the neuron to the left of the stimulation point fluoresces dramatically (t=64.5s). While not shown, this calcium wave oscillates back and forth between the left and right neurons for another ~40s before becoming saturated in both somas.

In Figure 5, the variation in fluorescence response with the laser pulse width is plotted. Each point represents the summed maximum fluorescence within the first four stimulation time intervals normalized to the maximum fluorescence during the experiment. The linear trend observed here shows that, with longer pulse widths, the fluorescence reaches saturation sooner. For 150 and 200ms pulse widths, the effects of photobleaching and calcium expulsion increasingly counteract the linear trend beyond the first two stimulation windows.

Several general observations from this set of data help elucidate the mechanism underlying the observed calcium fluorescence response: 1) the response is cumulative and delayed, 2) it continues beyond the laser stimulation period in some cases, 3) it scales with the duration and power of the laser pulses, 4) it propagates from the laser focus, and 5) it is irreversible within the time span of the background fluorescence rising to saturation (presumably caused by the broadband excitation light source releasing internal calcium stores).

We probed the mechanism further by conducting a series of pharmacological experiments designed to isolate various components of the cells. The first such experiment involved adding propidium iodide (PI) to the extracellular matrix, the results of which are shown in Figure 6. Relative to the unstimulated cells, this experiment clearly shows that photo-poration does indeed occur at the laser focus and that the cumulative effect is not self-healing at either power level; however, the time scale for significant influx varies from several minutes at 147mW to tens of minutes at 75mW. At 75mW, the laser irradiance is 2×10^{11} W/cm^2, which is below that necessary for bubble formation or cell damage, but still sufficient to induce stress and to ultimately porate the plasma membrane [7]. We speculate that the slower response observed when focused over the soma is most likely due to the greater capacity to self-heal there than along a process. However, unless a small amount of extracellular calcium triggers a cascading release of internal calcium, this mechanism alone is insufficient to produce the fluorescence activity seen here.

A second pharmacological experiment was conducted in the presence of zero extracellular calcium. Here, the fluorescence activity was dramatically reduced (data not shown), indicating that extracellular calcium is a major source of the resultant fluorescence response. Given this result and the slow photoporation mechanism, we attempted to isolate additional means of calcium entry. One possibility, through the heat-activated transient receptor potential vanilloid (TRPV) channels, was tested by adding the thermal channel blocker SB36671 to the extracellular matrix (data not shown). At 1μM, the activity was not significantly mitigated; whereas, at 10 μM, the blocker delayed but did not suppress the activity, indicating that thermal heating at and near the laser focus does in fact permit Ca^{2+} entry into the cell but is not solely responsible for the influx. Another possibility is that the opening of voltage-gated sodium channels (and the firing of action potentials) was responsible for the Ca^{2+} influx. In the presence of the sodium channel blocker, vinpocetine (in ethanol), the activity was delayed and reduced relative to normal conditions. This suggests that the sodium channels play a major role in the calcium response. Whether this leads to action potential firing cannot be determined without concurrent electrical measurements.

As a final pharmacological test, we introduced 5μM of thapsigargin, which blocks the SERCA-pump import of calcium into the endoplasmic reticulum (ER). The result was nearly complete suppression of the fluorescence activity (data not shown). This clearly demonstrates that the activity is dependent on the ER SERCA-pump loading and release of calcium. Therefore, based on these experiments, the proposed mechanism of opto-stimulation of neurons observed here is the result of an influx of extracellular Ca^{2+} at the stimulation spot through native membrane channels, both voltage-gated calcium and TRPV channels, that is subsequently loaded into the ER and then irreversibly expelled into the cytosol.

In contrast to the stimulated activity, the spontaneous Ca^{2+} spiking exhibited a distinctly different response. First, we observed that any cell within the FOV could display spontaneous behavior, not just the cell or cells clearly connected to the stimulated site. Second, the spiking occurred out-of-sync with the laser pulse trains and after a significant time delay (~2-4min.). In separate control experiments, we confirmed that spontaneous activity happened independently of laser stimulation entirely. Given the long delay, we speculate that the spontaneous response is triggered by the gradual increase in the baseline fluorescence, which in turn is likely the result of an internal release of calcium from the mitochondria caused by the broadband excitation source (465-500nm) [21]. Third, the temporal response of the spontaneous activity is much quicker than the corresponding stimulated activity. Rise times are on the order of a few seconds followed by decays times on the order of tens of seconds. Finally, the magnitude of the spontaneous response is generally smaller than the stimulated response and well below saturation, which also suggests an intercellular rather than an extracellular calcium release.

Femtosecond laser stimulation offers the ability to stimulate living neurons with high selectivity and minimal invasiveness. Here, we demonstrated a delayed, irreversible yet strong extracellular calcium influx triggered predominantly by the opening of membrane channels along the neural processes. This technique will enable the discovery of the role played by different neuronal cell types and networks and can easily be extended to multi-site stimulation with a spatial light modulator (SLM) or a galvo-mirror system.

2.1.5. Neuron Placement with Optical Tweezers

A major difficulty with *in vitro* cultures of dissociated neurons is the inability to control the network architecture of the neurons. This is crucial to our goal of assembling in vitro corticostriatal networks with user-defined architectures in order to examine the impact of network architecture on information processing. We previously demonstrated techniques [6] for embedding surface guidance cues into glass substrates in order to influence cell attachment and network outgrowth. Previously, we developed a similar cell guidance technology in which buried microchannels are embedded into glass substrates to guide primary neuron growth into pre-defined architectures (James et al., SAND2010-6486). But this technology still suffers from the inability to direct the initial neuron attachment in a non-random fashion, given the stochastic nature of neuron plating and the random distribution of neurons on a substrate entailed by that method. We examined the use of laser tweezers in collaboration with Walter Paxton (1132) as a method for direct cell-by-cell positioning of neurons onto substrates. Figure 7 shows an experiment in which two neurons were placed into guidance cue nodes that have been etched into a glass substrate. The glass substrate was inverted in an inverted microscope and coupled with a coverslip and gasket containing a solution of neurons in growth media. Once cells settled to the glass coverslip, the were grasped with the laser tweezers and moved up in z and around in xy and pushed into the glass substrate with guidance cues. After several neurons are similarly placed, the chip is rotated face up and then cultured in an incubator. We are currently exploring the viability of this method for fabricating user-defined networks.

2.2. Primary neurons in 3D hydrogel matrices

A major concern in experimental neuroscience is the biological relevance of dissociated neuron culture experiments. The loss of tissue structure and the plating of neurons onto artificial substrates that lack the biochemical cues necessary for neuron differentiation and maturation present problems for translating experimental results into potential clinical applications. As a first step towards improving the biological relevance of this effort, we examined the option of encapsulating primary neurons into hydrogels in order to provide a 3D environment for neuron growth.

2.2.1. Encapsulation of neurons in gels

A major concern for dissociated neuron culture is the survivability of the neurons, and this concern also remains with regard to the incorporation of neurons into 3D matrices. Diffusion of nutrients to and waste away from neurons in these environments is of vital importance. Here we show the first integration of rat primary cortical neurons within silica matrices that report viability following 7+ days of entrapment (Figure 8 and Figure 9). Primary neurons are difficult cells to maintain in culture, and they are extremely relevant for cell-based detection of toxic agents that target the nervous system. Creating cell-based sensors practical for defending the warfighter and personnel in less-developed or unstable regions requires a biocompatible interface between the cells and the macro world. Specifically, these cells require a functional bio-inorganic interface that allows cellular interactions at the nanoscale while maintaining viability.

We have developed a tool set for improving long-term viability and activity of integrated cells by tuning the silica matrix density, water content, addition of ameliorant compounds, media and nutrient content, silica matrix precursor chemistry, and silica delivery method (liquid sol, vapor phase, weakly condensed Si films). We have successfully used these tools to stabilize a wide variety of living cells, including mammalian cells, in our matrices. These tools allowed us to tune the bio-nano interface to cortical neuron cells, optimizing for long-term viability.

Specifically, we have found success using alkoxysilanes modified with diols or polyols for cellular encapsulation as these systems including high water solubility (no organic co-solvent required), initiation of hydrolysis and condensation reactions by the addition of water (no requirement of acid or base catalyst), and hydrolysis products that are biocompatible alcohols (i.e. glycerol). We have also found success using aqueous silica precursors (sodium silicate) that have been tuned to biologically compatible ionic conditions and pH.

In both cases addition of ameliorants was required to maintain cellular viability. Glycerol provided a significant enhancement in cellular viability. This is attributed to the high osmolarity of glycerol which decreases the activity of water, and can be transported through the cell membrane via aquaglyceroporins, modifying the membrane permeability. The formation of a high glycerol and water containing region surrounding cells entrapped in silica matrices has also been reported [22, 23], and that interface has been implicated in improved cellular viability. We have found that these attributes are crucial in stabilizing the relatively more fragile plasma membranes of mammalian cells compared to cells walls of yeast and bacteria. Also, we found significant enhancement in viability by including components commonly found in the extracellular matrix including collagen and gel from Engelbreth-Hol,-Swarm murine sarcoma.

Over the course of this study we have shown the ability to culture primary neurons on top of these synthetic silica matrices, with processes going into the matrix, resulting in 3D culture. This 3D culture is more analogous to behavior found *in vivo*; therefore, results obtained are more relevant than those from simple 2D culture. We have also shown the ability to stabilize cortical neurons cells at various stages of growth by introducing an encapsulating silica matrix on top of the cells. Cells remained viable following gelation and over 7+ days within the matrix. Cells and processes were physically restricted, preventing further growth/migration of cells and processes. This is important in studies where placement of cells and location of processes is critical, i.e. bioelectronics, biosensing, and fundamental studies in neural stimulation and inter/intra cellular communication. Finally, we showed that mixing of free primary cortical neuron cells within pre-gel solution, followed by gelation, resulted in viable cells encapsulated in the silica-biocomposite matrix. Further, by tuning the density of the matrix, we showed that cells could extend processes through the matrix and behave in a manner similar to cells found in natural tissues. This is extremely important in microfluidic system studies that serve as *in vitro* mimics for living tissue and organs for response testing to various chemical/biological stimuli. We are currently assembling this effort into a manuscript.

3. CORTICOSTRIATAL TISSUE NETWORK CHARACTERIZATION

3.1. Long-term depression in corticostriatal tissue networks

Synaptic plasticity underlies nervous system functions from signal processing to learning and memory. Short-term changes occurring in presynaptic neurons and in feedback circuits underlie the frequency dependency and instantaneous efficacy of transmission of action potentials through neuronal networks. Long-term changes in both the pre- and postsynaptic regions are thought to be the basis of learning and memory. The glutamatergic synapse between Layer V cortical projection neurons and medium spiny neurons in the dorsal striatum exhibits both of these forms of plasticity. Importantly, the corticostriatal circuit plays an important role in various forms of associative learning and in modulation of motor behavior.

We have previously investigated the role of D2 receptors in the induction of long-term depression (LTD) following a 100 Hz high frequency stimulus paradigm [24]. In addition, we have delineated the GABAergic feedback mechanisms responsible for the low-pass filter characteristics of this synapse [25]. In this study we further investigated the stimulus frequency and pattern necessary for LTD induction and the subsequent effect of LTD on the low-pass filter characteristics of this synapse. The following material is currently being prepared for submission to a journal for publication.

3.1.1. LTD Methods

3.1.1.1. Animals

All experiments were approved by the Institutional Animal Care and Use Committee at the University of New Mexico Health Sciences Center and conformed with NIH guidelines. Coronal striatal slices were prepared at the University of New Mexico from approximately 21 - 28 day old C57/Bl6 mice as previously described [26].

3.1.1.2. Electrophysiology high frequency stimulus paradigm

Briefly, animals were deeply anaesthetized by i.p. injection of 250 mg kg^{-1} ketamine (Fort Dodge Animal Health, Fort Dodge, IA, USA), brains were rapidly removed, and slices were cut at 300 μm with a vibroslicer (Pelco 101, St Louis, MO, USA) in an ice bath with a cutting solution containing (mM): 220 sucrose, 3 KCl, 1.2 NaH_2PO_4, 26 $NaHCO_3$, 12 $MgSO_4$,

$0.2\ CaCl_2$, 10 glucose and 0.01 mg ml^{-1} ketamine equilibrated with $95\%O_2$–$5\%CO_2$. Slices were then transferred to a bath containing artificial cerebrospinal fluid (ACSF) containing (mM): 126 NaCl, 3 KCl, 1.25 NaH_2PO_4, 1.3 $MgSO_4$, 26 $NaHCO_3$, 2.5 $CaCl_2$ and 10 glucose equilibrated with $95\%O_2$–$5\%CO_2$ at 30°C for 1 h and then maintained at room temperature (20 – 22°C) until transfer to a temperature-controlled recording chamber (Warner Instruments, Hamden, CT, USA), which was maintained at 32°C and continuously perfused at 2 ml min^{-1} with ACSF saturated with $95\%O_2$–$5\%CO_2$.

A concentric bipolar stimulating electrode (FHC, Bowdoinham, ME, USA) electrode was placed in the layer V cortical projection to MSNs in the striatum. Presynaptic constant current pulses (150 μs duration) were applied from a Master 8 through an Iso-Flex constant current stimulator (both from API Instruments, Jerusalem, Israel). fEPSPs were recorded with an Axoclamp 2B amplifier (Molecular Devices, Sunnyvale, CA, USA) and a Digidata 1322A interface using pCLAMP 8 software (Molecular Devices). Recordings were digitized at 500 kHz and filtered at 2 kHz. Population spike (PS) amplitudes were calculated by subtracting the average of both positive components in the fEPSP from the maximum intervening negative value

To assess long term synaptic plasticity in the corticostriatal field, a 10 minute baseline was established at ½ maximum stimulus intensity, then one of 6 high frequency stimulus (HFS) paradigms with stimulus pulses at either half maximum or maximum intensity was applied, and finally 30 minutes of recordings were obtained again at ½ maximum stimulus intensity. The average amplitude of the final 10 population spikes during the 30 minute period was compared to the average amplitude of 32 population spikes during the 10 minute pre-HFS baseline in order to determine the percentage of change relative to the baseline.

3.1.1.3. Electrophysiology Filtering Paradigm

The filter properties of the corticostriatal field were determined by an additional stimulus paradigm, which was applied before and after the assessment of long-term synaptic plasticity. In this random frequency train paradigm, 5 Hz to 60 Hz instantaneous frequency pulse trains were produced by a waveform stimulus file in Clampex. The uniform distribution of instantaneous frequencies for a 40 s period of this paradigm was determined by the following statistical tests: A Pearson's correlation of instantaneous frequency vs. time yielded $P = 0.383$ and $R^2 = 0.0279$

and a Spearman's correlation of the number of occurrences vs. binned instantaneous frequency yielded P = 0.340 and $R^2 = 0.0964$.

Frequency response data for PSs were fit with a 3rd order Butterworth low pass filter with a least squares regression using the Levenberg-Marquardt method in ProStat (v 6, Poly Software International, Pearl River NY) using Equation 1:

Equation 1:

$$\boldsymbol{V_{mean} = Alog_{10}(1 + \frac{Hz}{CoF}^{6})}$$

where: V_{mean} is the frequency-dependent gain that was fit to the average PS amplitude during the binned PS amplitudes generated by the random frequency protocol, Hz is the stimulus frequency, CoF is the cutoff frequency for a low pass filter, and A is a scaling factor that is directly proportional to the roll off of the filter. Statistical analyses were calculated using GraphPad Prism (GraphPad Software, La Jolla, CA). All drugs were purchased from Tocris Bioscience (Bristol, UK). Values of n represent slices.

3.1.2. LTD induction results

The induction of long-term synaptic depression in the corticostriatal synaptic field has been shown to involve both post-synaptic D2 receptors and feedback to presynaptic CB1 receptors. This induction repetitive firing of glutamatergic fibers that produces an initial post tetanic depression followed by a process, which we have called short-term depression (STD), that lasts for about 10 minutes. In some instances, a longer lasting, long-term depression (LTD) is induced, which is maintained for an excess of 30 minutes (Lovinger etc.). The first goal of this study was to investigate the characteristics of stimulus paradigms that led to STD vs. LTD.

Figure 10 shows a set of LTD data from a series of corticostriatal tissue slices. Panel A shows representative field excitatory post-synaptic potentials (fEPSPs) before and after high-frequency stimulus (HFS) is applied to the tissue. Short term depression (STD) occurs when the output signal measured in the striatum after HFS recovers to within 80% of the output signal amplitude measured before HFS. Long-term depression occurs when the output signal recovers to only 50% of the pre-HFS amplitude (Figure 10B). Figure 10C shows two experiments with different slices in which one exhibits STD and the other LTD. The time course of the recovery of the signal amplitude in the striatum is shown.

The 10 Hz, 3000 pulse paradigm at maximum intensity produced the greatest reduction in population spike amplitude of the 6 paradigms that we tested (Figure 11). The reduction in population spike amplitude produced by the 10 Hz 300 pulse paradigms was a result of a reduction in the amplitudes in the cluster that showed the least recovery (LTD) with little effect on the cluster with the greatest recovery (STD). Paradigms that included 400 stimuli at maximum intensity produce clusters with approximately equivalent means regardless of the underlying stimulus frequency (Figure 12); however the 10 Hz paradigm was the most reliable in producing LTD.

We tested the effect of LTD induction on the low pass filtering characteristics of this synapse and found that long-term synaptic plasticity had little effect on this important synaptic property (Figure 13). A 10 minute baseline (BL#1) was followed by a random stimulus paradigm (RS# 1), followed by a second 10 minute baseline (BL#2). Next a 10 Hz, 400 stimuli HFS paradigm was done followed by a 30 minute recovery period (RESULT). Finally, this was followed by an identical random stimulus paradigm (RS#2). Averages of the last 10 readings 30 minutes after the HFS were divided by averages of each of the 10 minute baselines to obtain the % of recovery of the pop spike following HFS. The average of recovery/BL#1 and recovery/BL#2 was used to then perform cluster analysis to obtain STD and LTD populations. 3rd order Butterworth low pass filter fits to random frequency stimuli either before or after 10 Hz HFS paradigm. Clusters (RS# 1 (grey), COF = 4.3688 Hz, A=0.0185, n=22; RS# 2 STD cluster (red): COF = 14.2026 Hz, A = 0.0370; n = 7; RS# 2 LTD cluster (green): COF = 3.4474, A=0.0084; n=15).

3.1.3. LTD Discussion

Long-term synaptic plasticity is generally accepted as a model of learning and memory. To be a valid model, this plasticity must be initiated by a physiologically relevant neural signal. HFS stimuli that mimic theta activity are commonly used to initiate LTP, but a similar association with the EEG power spectrum has not been made for LTD induction. We show here that extended HFS stimuli in the alpha range (8 – 13 Hz) are the most efficacious in inducing LTD in the corticostriatal synaptic field. Importantly, we show here for the first time that following HFS in synapses that are capable of sustaining LTD there is a reduced effectiveness of low pass filtering of subsequent signals.

4. NEUROMORPHIC MICROELECTRONIC DEVICE DESIGN AND FABRICATION

4.1. History of neuromorphic and analog-like microelectronic devices

Researchers have been seeking fundamental paradigm shifts in hardware for computation for several years. The power density limits and microprocessor-RAM bus bandwidth are primary obstacles with regard to maintaining the current hardware trajectory with an end goal of exascale (10^{18}) operations per second for supercomputers. In this section, we present several efforts to explore novel device hardware for computational purposes. The first effort was focused on utilizing a multiferroic material which affords both electric and magnetic polarizations for a total of two states within a single device [27]. By using complementary microelectrode configurations (surface and embedded), we were able to measure the in-plane and out-of-plane ferroelectric polarizations independently, thus providing additional characterization information on bismuth manganite thin films. The second effort is a theoretical conception article on simulating the impact of multi-layered insulator films on conductive filament based memristor devices [28]. In this work, we stack insulating films with contrasting ionic conductivities between two electrodes in order to modulate the growth of filaments within the structure. We predict improved performance for such devices in terms of linearity and controllability of switching. We also present here our initial efforts at fabricating such devices using Ag as our conductive filament within a multilayered structure of SiO_2 and TaO_x. Our next effort is a theoretical study in collaboration with Dept. 1748 and Hewlett Packard on tantalum oxide based memristors and the impact of the filament geometry on the switching dynamics [29]. This study also includes experimental data on HP-fabricated devices that comports with our theoretical model of oxygen vacancy flux within devices. The final portion of this section will cover two additional manuscripts on memristor switching dynamics and information storage that are currently in the process of being submitted.

4.2. Multiferroic devices for multi-bit memory storage

This work was accepted to the Journal of Applied Physics in 2013 and the material is included here [27]. Ferroelectricity is an active field of scientific inquiry due to both its complex physical origins [30] and its wide range of technological applications, including actuators[31], rf devices[31], and non-volatile memory[32]. As a result, there has been considerable progress in understanding the physics governing ferroelectric polarization, and complex models describing nucleation statistics[33] and domain growth/coalescence[34] have successfully reproduced domain switching phenomena spanning more than 8 decades of time[35]. However, while the temporal dynamics of polarization are well understood, the spatial characteristics are sparsely studied for many reasons including technical challenges involved in conducting polarization measurements. For instance, the experimental geometry used to probe ferroelectric materials is almost universally a tri-layer capacitor structure, meaning that measurements are sensitive to only a single component of the ferroelectric polarization vector. Neglecting the vector nature of polarization has become an increasingly relevant limitation, particularly in magnetoelectric and multiferroic materials, as novel coupling mechanisms have been shown to be sensitive to specific polarization orientations (e.g., polarization 'flops')[36-39].

Theoretical advances have clarified the calculation of ferroelectric polarization [40], and methods such as density functional theory [40, 41] and molecular dynamics simulations[42] have successfully described the vector nature of microscopic ferroelectric polarization. However, despite the need to understand polarization orientations, experimental methods to resolve the in-plane and out-of-plane polarization in ferroelectric or multiferroic thin films are not well established. Piezoresponse force microscopy (PFM) measures electromechanical responses which can be linked to local polarizations described by the piezoelectric and electrostriction constant tensors [43-45]. This approach allows domain structures to be successfully mapped with excellent resolution (10 nm lateral resolution and displacements of sub-pm) [46]. However, because the piezoelectric and electrostriction tensors are generally unknown, PFM is limited to qualitative descriptions of the polarization vector [47]. A quantitative description of the polarization vector requires a measurement of the charge transfer during a switching event, and the small size (typically 100x40 μm^2) of the probing cantilever renders measurements untraceable [47]. To address these limitations, we report here on measurements which quantitatively resolve the in-plane and out-of-plane polarization components of a thin film multiferroic by the use of two complementary interdigital microelectrode configurations: surface microelectrodes deposited on top of a multiferroic film and embedded microelectrodes where the multiferroic film and microelectrodes are adjacent to each other within the same plane.

4.2.1. Embedded microelectrode device structure

As described above, it is important to emphasize that the ferroelectric polarization is a vector quantity. Remanent ferroelectric polarization is limited to set crystallographic orientations, and does not simply align itself to the applied electric field; therefore, considering the relative microelectrode, ferroelectric film, and polarization vector orientation is vital to understand the component of the ferroelectric polarization that is measured. In bulk samples, placing large area electrodes in arbitrary orientations on the sample enables all components of the polarization to be measured. In fact, this is the method by which polarization 'flops' were first observed [36, 38]. However, thin films are less amenable to generalized electrode orientations, and are typically limited to measuring the z-axis (out-of-plane) component of the polarization. Additionally, the polarization orientation is generally unknown, prohibiting a trigonometric determination of the total polarization from a single component.

The out-of-plane component of polarization in thin films is commonly measured using a tri-layer metal-insulator-metal capacitive structure, allowing charge to be transferred vertically from ferroelectric domain switching. However, when thin films are required to be grown on insulating substrates such as $SrTiO_3$, the placement of a bottom electrode may be difficult due to lattice matching constraints, and surface interdigital microelectrode arrays are used instead [48]. In this configuration, the capacitor is composed of alternating V+/V- "finger" microelectrodes uniformly spaced on top of the film surface (Figure 14a). This structure produces fringing electric fields with equipotential planes intersecting the ferroelectric film between each pair of microelectrodes, and the area of the effective capacitor may be calculated analytically using conformal mapping and equating the capacitor thickness to half the electrode spatial wavelength [49]. This structure is also limited to measuring the z-axis out-of-plane polarization (P_{OP}) of the film due to the fact that the charge transfer that occurs during a voltage sweep only occurs at the film/microelectrode interface in the z-direction, and is therefore insensitive to charge motion within the plane of the film. Unique to this study, we have devised a complementary experimental method to quantitatively measure the in-plane ferroelectric polarization of thin films. By embedding the microelectrodes adjacent to the film of interest, a simple geometric area is obtained, thus allowing for direct, linear, in-plane electric fields within the device (Figure

14b). This geometry is selectively sensitive to the charge transferred due to the in-plane component (P_{IP}) of the polarization again due to the orientation of the film/microelectrode interface.

We have chosen the notation "in-plane" (P_{IP}) and "out-of-plane" (P_{OP}) to describe the polarization components, as opposed to the x-axis and y-axis polarizations (P_x and P_y). This notation was motivated by multiple reasons: First, our films are grown on cubic STO, which applies a biaxial compressive strain of 0.77%. Ferroelectric polarization is driven by structural distortions, therefore, the large biaxial strain strongly suggests that comparable distortions (and therefore polarizations) may be induced along either axis, and that it is likely that $P_x \approx P_y \equiv P_{IP}$. Second, the measurement of the individual polarizations P_x and P_y is experimentally challenging since ferroelectric polarization vectors can be oriented in multiple degenerate orientations within the structural unit cell, and will maximize their alignment with the applied electric field to minimize energy. Therefore, measuring P_x and P_y with separately oriented electrodes does not determine individual components, but rather measures transferred charge from different polarization vectors which have aligned themselves to the applied field orientations (see the reorientation of polarization vectors illustrated in Figure 14c). The individual components must be measured simultaneously under a single electric field orientation, which due to signal-to-noise requirements and limitations on the multiferroic film dimensions made this approach not feasible for this study. Therefore, we have reported our polarization vectors comprising two distinguishable 'in-plane' and 'out-of-plane' vector components.

For this study, we examined multiferroic (simultaneously ferromagnetic and ferroelectric) thin films of $BiMnO_3$ (BMO) grown with a <111> orientation on $SrTiO_3$ <001> via pulsed laser deposition [48]. An off-stoichiometric (Bi-rich) target with composition $Bi_{2.4}MnO_3$ was ablated using a KrF excimer laser ($\lambda = 248$ nm) with an energy density of 1.0 ± 0.2 J/cm^2. The optimum flowing oxygen pressure and substrate temperature, T_S, were found to be 37 mTorr and 632 °C, respectively, with deposition rates of approximately 0.05 nm/s. At the end of the deposition, the films were quenched in an O_2 atmosphere of 680 Torr at a rate of 20 ^{o}C/min. Interdigital microelectrodes were fabricated on top of the BMO films using methods described previously [49]. The interdigital microelectrode arrays were designed to have total areas of approximately $A_{\text{inter}} \approx 10^{-4}$ cm^2.

We examined the ferroelectric properties of these thin film samples by measuring *remanent* polarization hysteresis loops using a Radiant Technologies Precision LC Ferroelectric Tester. Typically, hysteresis loops are calculated by integrating the total transferred charge during application of a bipolar triangular voltage waveform, with contributions from leakage current, capacitance, and ferroelectric domain switching (remanent polarization). Alternatively, the polarization in a remanent hysteresis loop is calculated by removing the non-remanent components (i.e., leakage and induced capacitive charging) and isolating the charge transferred solely from ferroelectric domains. This is achieved by comparing two hysteresis loops that are preceded by alternate poling pulses. In the first loop, the domains are poled along the direction of the subsequent voltage sweep, ensuring that no charge can be transferred due to domain switching. In the second loop, the domains are poled opposite to the polarity of the subsequent voltage sweep, ensuring that all domains switch. The non-remanent charge transfer is independent of the pre-poling voltage pulse and is the same in both loops, therefore, the difference in polarization between the two loops is due to the *remanent* ferroelectric polarization. Our measurements are strictly *remanent* polarization charge transfer measurements (as opposed to induced polarization as in capacitance, see discussion above) which are normalized by the electrode area, and they are not affected by this subtlety of capacitive measurements.

Figure 15a shows a representative *remanent* polarization hysteresis loop measured via surface interdigital electrodes, with a quite large maximum value $P_R \approx 23\ \mu C/cm^2$ and coercive field of $E_C \approx 41$ kV/cm, confirming our sample is in fact ferroelectric. All measurements were made at 5 K, using a Quantum Design Physical Property Measurement System (PPMS), with measurement frequencies of 10 Hz. Figure 15b shows the magnetic characterization of the BMO films, demonstrating they are also ferromagnetic, and thus multiferroic. The magnetization was measured as a function of both temperature and magnetic field using a Quantum Design SQUID magnetometer. Zero-field-cooled (ZFC) and field-cooled (FC) warming curves both display a saturation magnetization of $M_{sat} \approx 1\mu_B$/Mn, measured under an in-plane ambient field of 1000 Oe. Magnetic field hysteresis loops show hysteresis with a coercive field of about 270 Oe observed at 10 K. The hysteresis observed in the M-H curves disappears and the M_{sat}-T trace displays a magnetic Curie temperature near $T = 80$ K.

With the surface interdigital microelectrode configuration, the out-of-plane polarization is measured. For assessing the in-plane polarization, we fabricated samples with microelectrodes embedded within the BMO film. Briefly, 60 nm of BMO were deposited on STO (as described above) followed by coating with a photoresist (AZ4110). The photoresist was then patterned using a Karl Suss MJB3 contact aligner for 10 seconds at an energy of 400mJ/cm^2. Patterns were then transferred into the BMO film via argon ion milling (VEECO/INTLVAC AM600, 300W, 33% duty cycle). Patterns were designed with widths and separations of approximately 5 µm. The photoresist mask was kept in place for the electron beam evaporation of an adhesive layer of titanium (10 nm) and then gold (50 nm). Substrates were then subjected to a lift-off procedure using N-Methyl-2-pyrrolidone (NMP) in a mega-sonic bath to remove the photoresist and leave the gold microelectrodes embedded in the BMO film. The sample is then cleaned with acetone/isopropanol, and water. Samples prepared for focused ion beam serial sectioning and scanning electron microscopy imaging were then coated with gold to reduce charging and with several micrometers of Pt to protect the device during milling. Samples were then milled and imaged with a FEI Helios Dual Beam microscope.

Figure 16a shows a scanning electron micrograph image of an embedded microelectrode device. Figure 16b shows a cross-sectional image of the embedded interdigital microelectrode arrays. Each embedded electrode "finger" has a length of L ≈ 2 mm long, and conforms to the h ≈ 60 nm thickness of the film. Within our electrode array, we have approximately $N = 30$ pairs of V+/V- electrode "fingers", resulting in a total area of, $A = N \cdot L \cdot h = 7.2\text{x}10^{-5}$ cm^2. It is important to note, that while the accurate calculation of *capacitance* based on the parallel plate geometry requires large aspect ratios such that *h/d* >> 1 (where *d* is the separation of the electrodes), the calculation of the electrode *area* is independent of the aspect ratio and is exact.

Figure 17a shows the remanent polarization loops measured for out-of-plane (red) and in-plane (green) polarization at $T = 5$ K. Both components show large polarizations, of $P_{OP} \approx 23$ µC/cm^2, and $P_{IP} \approx 12$ µC/cm^2 (although saturation could not be achieved in this electric field range for P_{IP}). Both polarization components display similar coercive fields, E_C, centered at approximately 42.5 V/cm and 50 V/cm for P_{OP} and P_{IP}, respectively. However, P_{IP} displays significant broadening of $E_{C,}$ suggesting that a significantly larger distribution of coercive fields exists in this component. This interpretation is understandable when considering the AFM image shown in Figure 15a which shows that the BMO films exhibit island growth morphology. Island edges can have diverging strain gradients [50], which result in modified electrical properties. In the in-plane polarization measurements, the electric fields cross a large number of islands, with large variations in the voltage drops across them. Alternatively, the electric fields for the out-of-plane polarization switching are primarily vertical (in the z direction), and thus traverse a maximum of 60 nm, which nominally corresponds to roughly 1 to 2 island widths.

By using both microelectrode configurations and independently measuring both the in-plane and out-of-plane polarization of a material, the total polarization (P_{TOT}) of the material may be determined by combining their components geometrically. Figure 14c shows this combination of polarizations, with the total polarization, $\boldsymbol{P_{Tot}}$, calculated as:

Equation 2:

$$|\boldsymbol{P_{tot}}| = \sqrt{\boldsymbol{P_{IP}^2} + \boldsymbol{P_{OP}^2}}$$

As seen, the calculated total polarization has a maximum of $\boldsymbol{P_{Tot}} \approx 27$ μC/cm^2, and is approximately 16% larger than the value originally measured by P_{OP}. Finally, comparing the relative sizes of the components also allows the orientation of the ferroelectric polarization to be estimated as,

Equation 3:

$$\boldsymbol{\tan^{-1}\frac{|P_{OP}|}{|P_{IP}|} = \tan^{-1}\frac{23\ \mu C/cm^2}{12\ \mu C/cm^2} \approx 62^o.}$$

In summary, we have presented a technique for resolving multiple spatial components of the remanent polarization vectors in thin film ferroelectrics. Using complementary electrode configurations of surface and embedded interdigital microelectrode arrays, we measured both the in-plane and out-of-plane polarizations. $BiMnO_3$ was shown to have a total ferroelectric polarization of $P_{Tot} \approx 27$ μC/cm^2 and magnetic polarization of $M_{sat} \approx 1\mu_B$/Mn, deeming these samples strongly multiferroic. As a result of the complementary electrode measurements, we find that the ferroelectric polarization vector is in fact 16% larger than what typical measurement geometries would report, which due to lack of saturation in P_{IP} represents a lower bound polarization missed by conventional measurements. The spatial sensitivity exhibited by the method presented here is important, as novel coupling mechanisms have been shown to couple to and modify specific ferroelectric polarization vector components.

4.3. Multilayered memristor devices with engineered conduction fronts

This work was published in the European Physical Journal of Applied Physics in 2013 and the article material is included here [28]. Resistive switching in materials via electric and magnetic fields has an extensive history of research [51-54], and is a key aspect of several technological applications [55, 56]. Resistive switching under applied voltage was first observed many years ago [57, 58], and following recent experimental work [59] has been connected to the fundamental theoretical prediction of memristive systems [60, 61]. Due to their non-volatile properties, scalability, and speed, memristors have been identified as a candidate for the replacement of flash memory. Memristors have also been seen as a potential component in next generation "neuromorphic" circuits that mimic biological neural networks to reduce the power consumption and hardware footprint for next-generation high performance computers [4, 62, 63]. However, significant limitations remain such as device-to-device reliability (which limits large scale production) and strongly non-linear switching properties (which limits the ability of memristors to emulate biological synapses). Here, we introduce a novel memristor design which increases the resistance modulation window and precision, and reduces device-to-device variations in resistive properties. By engineering a uniform conduction front (UCF), the variability of the resistive switching decreased by as much as 90%, and the window of resistance modulation with controllable linear tunability increased by as much as 75%. Furthermore, the attainment of a UCF increases the memcapacitive properties of the device by as much as 400%, enabling additional applications such as dynamic RF filtering, or efficient digital computation [64].

4.3.1. Engineered conduction fronts in filamentary memristor devices

Two classes of memristors have garnered particular interest [56]: the electrochemical mechanism class (ECM), and the valence change mechanism class (VCM). The resistance switching in both classes is driven by ionic transport through an insulating matrix under an applied electric field. In the ECM class, an active electrode donates electrochemically active ions (Cu, Ni, or Ag) which reduce/metalize once they diffuse to an opposing inert electrode (Pt, W). In VCM systems, oxygen vacancies are the mobile ions, which dope oxide layers resulting in higher local conductance. Figure 18a shows a schematic of the basic structure of a filament-based memristor device. When a voltage is applied between the top and bottom electrodes, mobile carriers drift through the insulating matrix under the electric field. Eventually, these carriers form conductive filaments that connect the electrodes resulting in a sharp reduction in resistance. Due to the stochastic nature of filament formation, these conductive filaments have random lengths and distributions [51, 56, 65, 66]. TEM studies of VCM and ECM resistive memory devices reveal multiple partial filaments in a single cross sectional slice, with evidence suggesting that the number of filaments is proportional to the length-scale of the device [67, 68]. Thus, devices with xy areas of hundreds of μm can contain hundreds of such filaments of varying lengths. Electric field strengths are higher (and thus growth rates are faster) for longer filaments due to their closer proximity to the target electrode. Thus, small statistical fluctuations in filament growth early in the process are magnified for longer filaments, further increasing their separation from shorter filaments. The net result is a length distribution of filaments that is highly non-uniform, with one long filament that shorts between the electrodes and a large population of short filaments (Figure 18b). This non-uniform "conduction front" of filaments results in devices with switching properties that strongly depend on random variations within the insulating matrix.

4.3.2. Filament model in single and multilayered memristor devices

Here, we show that by incorporating specifically spaced layers with contrasting ionic conductivities, the electric field amplifications can be offset, and a more uniform front of conductive filaments can be produced. We begin by modeling a simple resistive switching event. Growth rates are determined for 100 independent filaments of length l_n (where n = 1:100) according to an activation model in which filament lengths increase as ions preferentially hop toward the filament tips under applied bias [56, 69-71]:

Equation 4:

$$\frac{\partial l}{\partial t} = d\,\omega\left(e^{\frac{-qU_a + qVd/2(h-l)}{k_B T}} - e^{\frac{-qU_a - qVd/2(h-l)}{k_B T}}\right) \qquad (a)$$

$$\frac{\partial l}{\partial t} = \mu E_0 \sinh\left(\frac{E}{E_0}\right) \qquad (b)$$

In Equation 4a, d is the hopping site distance, ω is the characteristic ion hop attempt frequency, U_a is the activation potential, V is the applied voltage across the insulating matrix (1 V), h is the thickness of the device, l is the filament length, k_BT represents the thermal energy, q is the ion's charge, and the negative term accounts for reverse hopping. Equation 4b offers a conceptually simpler representation where the prefactors are combined into an effective mobility, $\mu = q\omega d^2 exp[-qU_A/k_BT]/k_BT$, and characteristic field, $E_0 = 2k_BT/(qd)$ $(E = V/(h-l))$. The large, non-physical hopping distances derived from activation models, $d \sim 3$ nm [56], have led some to suggest that linear ionic drift in an electric field may be more plausible, therefore we have also repeated our simulations using a linear ionic drift model and obtained similar results. The simulated filaments grow uniaxially through an ionic conducting medium in which the ionic mobility at each point is determined by a Gaussian distribution in order to emulate local irregularities such as grain boundaries, interstitial atoms, trapped charge, and other factors. Figure 18c is a schematic of a multilayered structure with materials with different ionic mobilities ($\mu_1 \neq \mu_2$). Two important factors in the simulations are the ratio of the layers' ionic mobilities and the z-dimension spacing and arrangement of the layers. Figure 18d shows a simulation of the filament length distribution for a multilayered device, and as shown, the filament length distribution is more uniform, with a substantially increased average normalized filament length (79±12% of the insulator thickness, h) compared to the single layer device (40±45% of h). The working principle is that the low mobility layers temporarily slow the growth of longer filaments, allowing shorter filaments to advance. Thus, the difference in filament lengths is reduced, and the longer filaments no longer have the same 1/d electric field (and therefore growth rate) advantage, allowing the shorter filaments to maintain comparable growth rates.

The uniform conduction front in the multilayered device has a substantial effect on the resistive switching properties. Figure 19b compares the resistive switching of a single ionic conductor memristor, and the multilayer device proposed here. The total device resistance is calculated by placing 100 classical geometric resistances in parallel, where each resistance is determined by: $R = \frac{\sum \rho_n L_n}{A}$, where ρ_n is the resistivity of each ionic conductor layer, L_n is the total thickness of all layers of that ionic conductor between the filament tip and top electrode, and A is the area of the memristor structure In the single ionic conductor memristor (blue), there is an initial range of linear resistance modulation, however, the majority of the resistive switching range, $\Delta R = R_{OFF}-R_{ON}$, is dominated by a rapid strongly non-linear resistance drop caused by the rapid growth of a single high conductance filament. This abrupt switching and the resulting abbreviated switching range limits the ability to precisely tune the device to multiple stable resistance values, which is a key element of analog and neuromorphic computing applications. However, in the multi-layer, alternating ionic conductor memristor (red) the uniform conduction front extends the range of linear resistance modulation to as much as 75% ΔR, which coincidentally is a ~ 75% increase in the tuning range (compared to ~ 44% ΔR for memristors with only a single ionic conductor layer).

The performance of the proposed multilayered device was investigated by modifying the thickness, and a custom unitless parameter called ‘layer-configuration’ (comprising number and spacing) of the alternate ionic conductor layers. A visual description of layer-configuration is provided in Figure 19a. With multiple layers, the number of design parameters can increase quickly. Therefore, for simplicity we start with equal thicknesses and map the position of the alternate ionic conductor layers using a generic power-law concentration profile: $c(z) = z^n$ (with results similar for most $|n| > 1$). Using this profile, the number of layers specified determines their positions. The position of each i^{th} layer for a given layer-configuration number (LC) are determined by:

Equation 5:
$$\int_{z_{i-1}}^{z_i} c(z)dz = \frac{1}{LC}$$

where i = 1:LC (in integer steps), and z_i represents the height of the i^{th} layer along the z-axis (with $z_0 = 0$). For example, with 3 layers, the first layer is centered at the x_1 position where the integral of $c(x) = 0.33$. Figure 19b shows a simulation of a device with a characteristic resistive switching event. The resistance and time are both normalized to compare the linear tuning range of resistance for different device designs. Parameters for this simulation were chosen to maximize the increase of linear tuning range as well as decrease the device-to-device variability (layer-thickness of 20% of the device thickness and layer-configuration of 1.6). Figure 19c shows the design space for optimizing the increase in the linear resistance tuning range. As the number of alternate ionic layers increases, the ionic mobility contrast decreases and approaches a single layer device, with an optimal design found between the two limits of single layer devices of either ionic conductor.

The design phase space contours are also sensitive to the material properties of the ionic conductor layers, and the characteristics of the alternate ionic conductor layers introduce additional potential design variables: the ratio of ionic mobilities (μ_2/μ_1), electronic resistivity (ρ_2/ρ_1), and dielectric permittivity ($\varepsilon_2/\varepsilon_1$) of the alternate ionic conductor layers. For the design phase spaces shown in this study: $\mu_2/\mu_1 = 1/100$, $\rho_2/\rho_1 = 1/2$, and $\varepsilon_2/\varepsilon_1 = 1$. Similar results were obtained for simulations with $\rho_2/\rho_1 = 1$. However, because ionic mobility correlates inversely with electronic conductivity, a value less than one was chosen.

The uniform conduction front not only affects the memristive properties of the device, but the memcapacitive properties as well. Memcapacitive systems are analogous to memristive systems; capacitance values are modulated by applied voltages and retained after their removal. Figure 20a shows the capacitance of a multilayered device as a function of time under applied bias. The tunable range of capacitance increases as much as 400% in multi-layer devices. The same 2-dimensional design phase-space spanned by layer-configuration (LC) and layer-thickness was investigated to optimize memcapacitive properties.

In addition to improving the range of linear resistance modulation and amplifying the memcapacitive properties, the alternating ionic conductor design is also predicted to reduce device-to-device (DTD) variability. We simulated the switching of different devices by running multiple simulations ($n = 1000$) with independent Gaussian distributions of local ionic conductivities in order to calculate the standard deviation of the range of resistance modulation for a large population of simulated device switchings. Figure 21 shows the design phase space for the device-to-device variation as a function of layer thickness and configuration. The standard deviation of the linear range of resistance was calculated and was shown to be reduced to as little as 10% of the variability observed in single layer devices (a 90% reduction).

4.3.3. *Implications of multilayered memristor structures*

The multi-layer alternating ionic conductor memristor design proposed here and its resulting uniform conduction front are predicted to provide substantial improvement in memristor device performance. The uniform conduction front facilitates fine-tuning of the resistance state, opening the possibility for analog and multi-bit applications. The uniform conduction front simulations also produced consistent switching events and demonstrated that the alternating ionic conductor design dampens the statistical variability inherent to device fabrication and operation. This is an important design feature, as DTD consistency and yield are major hurdles to large scale memristor production [72, 73]. Furthermore, this design paradigm could result in specific new applications for resistive switching. By selecting layers with specific resistivities, the switching profile itself may be designed with almost any monotonically decreasing function theoretically possible. For analog applications such as neuromorphic computing, designing specific non-linear switching profiles could be useful to emulate particular learning rates due to varying synaptic development throughout the brain.

The amplification of the memcapacitive properties is of particular interest, as memcapacitive research is relatively fledgling [74], and thus far, memcapacitive properties have only been proposed/demonstrated in select systems: ionic nanopores [75], floating gate superlattices [76], elastic membranes [77], and phase change systems [78]. Strong limitations on the memory of the memcapacitive properties have been typical, such as: limited frequency ranges, chaotic behavior, or sharp temperature boundaries centered on phase transitions. Importantly, the multi-layered memcapacitive structure proposed here is predicted to operate with fewer of these limitations while retaining high stability and independence from frequency and temperature.

Given the design space explored above, future work includes the fabrication of test structures to validate the simulations reported here. Candidate materials such as binary metallic oxides (SiO_2, Ta_2O_5) for low mobility layers, and chalcogenides (GeSe, GeS) for high mobility layers are promising and are currently being explored. Considering the configuration-thickness phase space of Figure 19c and Figure 20b, we see that designs with as few as 1 to 2 additional layers with thicknesses of approximately 20% to 50% of the total device thickness demonstrate significant device performance improvements. For a reasonable memristor thickness of 50 nm, this implies layers of 10 nm to 25 nm, which can be easily obtained with standard microfabrication tools. The alternate ionic mobility can be obtained by introducing interstitials or varying grain boundaries concentrations by altering the temperature and ambient pressure during growth. Additionally, by selecting materials with different annealing temperatures, grain boundaries may be selectively removed in one of the two ionic conductors via annealing, providing direct layer-selective tuning of ionic mobility.

In summary, we have presented a novel design for memristive/memcapacitive structures in which the conduction front may be engineered to be quasi-uniform by introducing layers of alternate ionic mobility which counteract the electric field amplifications of filament growth. The uniform conduction front was predicted to increase the memristive and memcapacitive switching ranges, as well as improve device-to-device consistency. This work provides an important step toward the design and manipulation of the conduction front within memristive/memcapacitive systems, an important capability to ascertain the true potential for this technology in future memory hardware.

4.4. Design and fabrication of multilayered resistive memory devices

In order to test the device structure hypothesized in Section 4.3, we designed a set of structures with multiple layers of insulators with varying ionic conductivities. We have examined GeSe insulator structures as well as devices with silicon dioxide and tantalum oxide insulator structures.

4.4.1. Germanium selenide / silver resistive memory structures

The GeSeAg filamentary system has been widely explored, thus we began our first experimental study of multilayered structures using this particular formulation. Tungsten or platinum (100nm) was blanket-coated onto oxidized silicon wafers to serve as the bottom electrochemically-inert bottom electrode (Figure 22). A shadow mask was then used to deposit isolated dots of GeSe (40nm Ge, 8.4nm of Se) onto the wafer. This was then followed by the evaporation of Ag (10nm) onto the GeSe dots. Figure 23 shows a switching event in a GeSeAg device (panels 1-6). When a positive voltage is applied to the top electrode, positively-charged silver ions drift under the electric field through the insulating GeSe matrix and make contact with the bottom electrode, switching the device to a low resistance state. It is important that the bottom electrode be inert, thus our use of platinum to prevent any electrochemical reactions from occurring between the silver ions and Pt metal. In the IV sweep, the resistance of the device is now in a lower state (position 4). As the voltage is swept back and turned negative, silver ions drift back to the top electrode and the device switches off (position 6).

4.4.1. Multilayered resistive memory devices

Figure 24 shows a schematic of the thin film stack for multilayered memristive devices to test the predictions made in Section 4.3. The silver electrode serves as the electrochemically active microelectrode. We also included a silicon dioxide layer doped with silver in order to increase the probability of filament extension through the insulating matrix. The full stack is shown here (TiAg – 28nm thick, TiPt – 53nm) – we also fabricated several control film stacks in order to assess the impact of stacking layers of different oxides: SiO_2 (15nm), TaO_x (12-14nm), $SiO_2/TaO_x/SiO_2$, and $SiO_2/TaO_x/SiO_2/TaO_x$. Figure 25 shows an example IV curve for a single TaO_x layer control device with a 20x20 μm^2 active area. This device design exhibited a very low reset voltage with an R_{OFF} = 10-20 kΩ and an R_{ON} = 500-800 Ω. Figure 26 details the IV curve for a 100x100 μm^2 active area device with a single SiO_2 insulator layer. Impedance spectroscopy of these films enables us to probe the electrical properties without switching the devices. Devices with a single layer of SiO_2 with 20x20 μm^2 active area displayed an initial capacitance of 96pF. When switched with a DC pulse, the device became purely resistive with a resistance of ~100Ω. After a reversed DC potential to switch the device back off, the device displayed characteristics of a parallel RC circuit with R=359MΩ and C=93pF.

4.5. A physical model of switching dynamics in tantalum oxide memristive devices

This work was published in Applied Physics Letters in 2013 and the article material is included here [29]. Memristive systems, which display hysteretic I-V relationships based on tunable internal state variables, were originally observed and predicted as many as 40 years ago [58, 60, 61, 79], but have recently become a field of intense research [52, 55, 56, 77]. Their inherently coupled ionic and electronic transport properties have provided fundamental research interest[71, 80], and their unique switching properties have opened up the potential for new platforms of functionality such as stateful logic operations [81] and neuromorphic computation [62-64]. However, in order to realize the aforementioned applications, optimal material systems (and their state variables) must be identified, and quantitative models of the physical mechanisms governing their resistive switching must be developed, allowing the resistive state to be predictively modulated, facilitating their integration into functional systems.

TaO_x memristors have recently shown fast switching on the sub-nanosecond timescale, and record endurance of more than 10^{12} cycles [82, 83] – which is believed to be linked to TaO_x's simple oxide phase diagram[84] including only two thermodynamically stable states: metallic Ta, and insulating Ta_2O_5. Similar to TiO_2, the motion of oxygen vacancies and the development of a conductive filament have been discussed; however, their exact role in the switching mechanism is still under debate with concern that their role changes depending on the device structure. In TaO_x memristors composed of a bilayer of Ta_2O_5 and TaO_x, qualitative models have shown that oxygen vacancies may behave similar to TiO_2 in which a vertical motion of vacancies provides local doping and tunes a Schottky tunneling gap [82, 85]. Conversely, in bilayer memristors of TaO_x and Ta, the lateral motion of oxygen vacancies or anions is thought to be key, with the oxygen concentration of a Ta rich conducting filament the purported state variable[83, 86]. Quantitative models describing the physics of phenomena such as retention have been demonstrated[87], however, as summarized above, modeling of the physics of switching dynamics in TaOx memristors has been primarily qualitative. Here, we present a model based on microscopic ionic flux which quantitatively predicts the memristive operation of TaO_x/Ta devices, providing close agreement with experimental resistive switching data.

4.5.1. Filamentary memristor device structure and operation

The material stack of our dot capacitor memristor is shown in Figure 27a. The films were grown via reactive sputtering with lateral dot-capacitor dimensions of 100x100 μm. Electrical contact was made to the top electrode of the devices using micromanipulator probes and a backside contact through the probe station chuck which substantially limited any series resistance, ensuring the entire voltage is applied across the device thickness. Virgin devices were electroformed with currents of approximately 5 mA and the memristive switching was characterized using an HP 4156C parameter analyzer with the pulse generator expansion unit. Data was obtained on approximately one hundred dot capacitors, all of which showed results similar to those presented here.

Figure 27b shows a typical hysteresis loop (measured in a two-terminal configuration) in which the device is reversibly switched between two stable states by applying positive and negative voltages, with $R_{OFF}/R_{ON} > 10$. In ON switching, the device gradually decreases resistance after a positive threshold voltage of approximately V = 0.5 V on the top electrode (bottom electrode grounded), whereas OFF switching is delayed to larger voltages ($V = -1\ V$) but occurs much more rapidly. To complete a more detailed electrical characterization we have also utilized a pulse/read measurement procedure in which a large state changing voltage pulse is applied, followed by a small, non-perturbative read voltage pulse which probes the device resistance state (50 ms, 1 mV, see Figure 27c inset). The curve in Figure 27c represents the resistance values measured following successive state changing pulses of a constant amplitude and width. Neglecting the time required for the read measurement, we interpret the data as the real-time evolution of the device resistance state under an applied constant voltage bias. The resistive switching curve in Figure 27c reaches an asymptotic value (which is dependent on the amplitude of the applied state changing voltage pulse – this suggests that the dynamics in these devices are not adequately captured by a simple integral of voltage or current flux[61, 79].

To accurately describe the resistive switching dynamics shown in Figure 27c, we have derived a quasi-3D model describing the time-evolution of memristive switching by predicting the change of a single state-variable dependent on three components of ionic flux: Fick diffusion, drift, and the less well known phenomenon of Soret diffusion [88, 89]. Soret diffusion, also referred to as thermophoresis, is the movement of molecules along a temperature gradient and is commonly observed in liquid/molecular solutions[90], however, its role in solid oxides has recently been emphasized[55, 89, 91]. Using these components of ionic flux, we find that the resistive switching can be reproduced by modulating the radius of a Ta-rich conducting cylindrical filament surrounded by a matrix of insulating forms of tantalum oxide.

4.5.2. Phase change in the oxide material during switching

The geometry of our model is inspired directly from experimental results [83, 86], and is shown in Figure 28. As observed in synchrotron x-ray fluorescence experiments, a Ta-rich conducting filament is surrounded by nano-crystalline Ta_2O_5 [83, 86]. Additionally, electron energy loss spectroscopy characterization indicated that an oxygen concentration gradient connects these two regions [83], which we represent by a sub-oxide phase, TaO_X , with a radially increasing oxygen concentration. Finally, because the majority of the current flows through the Ta filament, we include a strong thermal gradient representing the expected ΔT between metallic and oxide regions caused by Joule heating. Defined in cylindrical coordinates with $\hat{z}$ and $\hat{\varphi}$ symmetry, the model predicts the lateral translation and modification of this sub-oxide phase, which subsequently alters the conducting filament radius.

Because the switching region is surrounded by asymmetric electrodes with unequal ionic mobilities (Ta, and Pt), under positive and negative bias applied to the Ta electrode, drift causes oxygen ions to flow in (OFF switching) and out (ON switching) of the switching region vertically ($\hat{z}$), and results in the increase and depletion of oxygen, respectively. Assuming the concentration profile remains relatively constant, this flux results in the lateral motion of the sub-oxide phase. Our model quantifies this lateral shift by calculating the number of oxygen ions required to increase a volume, ΔV, to the oxygen concentration of the adjacent Ta_2O_5 phase ($\Delta V = 2\,\pi\, r\, L\,\Delta r$, where L is the film thickness). The number of oxygen ions (N) that have been transported to the filament can be estimated by integrating the ionic flux over area and time ($N = \Delta t \int \boldsymbol{J}_{Tot} \cdot \boldsymbol{dA}$). This change in oxygen concentration leads to a corresponding shift of the sub-oxide phase and thus a change in the filament radius. Using the definition of concentration, $n = N/\Delta V$, the resulting change in filament radius may be written as:

Equation 6:

$$\Delta r = \frac{\Delta t \int J_{Tot} \cdot dA}{2\pi r L n}$$

As mentioned above, in our model J_{Tot} comprises three components corresponding to Fick diffusion, Soret diffusion, and drift: $J_{Tot} = J_F + J_S + J_D$, with:

Equation 7a,b,c:

$$J_F = D\,\nabla n$$

$$J_S = DS\,n\nabla T$$

$$J_D = Dn\,Eq/(k_B T)$$

where D is the diffusion coefficient [89], ∇ represents a spatial derivative, S is the Soret coefficient defined as the ratio of the thermodiffusion coefficient, D_T, to the normal diffusion coefficient, D [89], T is the temperature, E is the electric field, q is the ionic charge, and $k_B T$ is the thermal energy. In this geometry, the Fick and Soret diffusion terms will be directed through the radial surface area of the filament: $dA_r = 2\,\pi\, r\, L$. We neglect the vertical Fick diffusion given the observed absence of a vertical oxygen concentration in the switching layer [83]. Here, Fick diffusion drives oxygen ions toward the conducting channel and Soret diffusion drives them outward. The drift is directed primarily along $\hat{z}$, and acts over the area of the oxide, $dA_z = \pi(r_{Tot}^2 - r_F^2)$, where r_{Tot} is the total radius of the entire switching region including the filament, the sub-oxide region, and the Ta_2O_5 region.

Despite the flux of oxygen anions from drift translating across the sub-oxide region, it is the two lateral diffusion components (J_F and J_S) which ultimately determines a steady state filament radius and resistance state of the device. The steady state radius, r_{ss}, is determined by the balance between these two competing forces, such that, $J_F - J_S = 0$ as the temperature and concentration gradients evolve. Therefore, the applied voltage enables bipolar control by indirectly modifying the balance between J_F and J_S, and forcing the system to establish a new steady state filament radius.

By considering infinitesimal time intervals and volumes, we see that Equation 6 can be rewritten in terms of the time derivative of the filament radius, and can be interpreted as the dynamical state equation of a canonical memristive system [60, 61, 92].To solve this equation we must have explicit expressions for J_F and J_S (and therefore, $\nabla \mathrm{n}$ and $\nabla \mathrm{T}$). For simplicity we assume a constant temperature difference between the filament and surrounding oxide, with uniform heat generation and vertical heat flow within the filament. For concentric cylinders with a temperature difference between their interfaces, the analytic solution for the temperature profile is known : $T(r) = \Delta T\left(1 - ({}^{r}/_{r_F})^2\right) + T_0$, which implies that, $\nabla \mathrm{T} = -2\Delta \mathrm{T}\, \mathrm{r}/\mathrm{r}_\mathrm{F}^2$, where r_F is the radius of the inner cylinder (the filament). Evaluating this gradient at the edge of the filament where growth occurs, $r = r_F$, we see that: $\nabla T \propto 2\,\Delta T/r_F$. While an oxygen concentration gradient was observed experimentally, its exact functional form is not known. Therefore, for simplicity we assume a concentration profile such that, $\nabla n \propto \Delta n/(r_{Tot} - r_F)$, which has the expected boundary conditions of starting small near $r_F = 0$, and increasing as $r_F \rightarrow r_{Tot}$ (where r_{Tot} is the radius of the nanocrystalline Ta_2O_5 region) , preventing runaway filament growth. Substituting these expressions into (1) produces:

Equation 8:

$$\frac{dr_F}{dt} = \frac{2DS\Delta T}{r_F} - \frac{D\Delta n/_n}{r_{Tot}-r_F} \pm D|E|q\left({}^{r_{Tot}^2}/_{r_F} - r_F\right)/(2\, L\, k_B T)$$

Unfortunately, there is no closed-form analytic solution for differential equations of this form, and $r_F(t)$ cannot be solved for directly. However, considering the limited range of filament radii expected ($R_{OFF}/R_{ON} \approx 10$, suggests a ratio of radii in the OFF and ON states, $r_{F,OFF}/r_{F,ON}$, of almost 3) it is possible to replace each term with a second order expansion in terms of r_F. Grouping the coefficients from each power of r_F, we see that a solution exists over our limited range,

Equation 9:

$$\int \frac{d\boldsymbol{r_F}}{\boldsymbol{a+b\,r_F+c\,r_F^2}} = \int \boldsymbol{dt}$$

where $a = \sum a_i$, $b = \sum b_i$, and $c = \sum c_i$, and a_i, b_i, and c_i are the coefficients of the 2nd order approximation of each ionic flux term. Integrating and solving for $r_F(t)$, we find:

Equation 10:

$$\boldsymbol{r_F(t) = r_0 + \Delta r\ \tan(\varphi + t/\tau)}$$

where $r_0$is the initial filament radius, Δr represents the total change of radius, τ is the switching time-scale, and φ is a phase factor.

4.5.3. On/Off switching as a function of pulse stimulus

With the dynamical state variable equation now derived and its time-dependent solution found, to complete the Chua memristor formalism, the static transport equation must be specified as well. For the data shown in in which the resistance is calculated from a single low voltage read measurement, the resistance of the device can be accurately reproduced assuming all the current flows through a cylindrical filament as suggested above, leading to: $I = V\pi r_F^2/\rho L$ (with $R = \rho L/\pi r_F^2$). Combining this approximation with a normalization scheme, the memristive switching data shown in Figure 29 were fit using only 3 free parameters, varying Δr, φ, and τ in Equation 10. This combination of simplicity and accuracy is compelling, as general functions such as exponentials produced poor fits, suggesting that the data has a unique curvature which is captured by our mathematically simplified model. For ON switching (0.65 to 1V), the fitting parameters smoothly varied across ranges of: $1.1\,nm < \Delta r \pm 0.3 < 5.3\,nm$, and $1.51\pi < \phi \pm 0.03\pi < 1.55\pi$, $54.4\ \mu s < 2\pi\tau \pm 11.3\ \mu s < 221\ \mu s$. For OFF switching, the range were: $-6.5\,nm < \Delta r \pm 1.9\,nm < -1.4\,nm$, $1.5\pi < \phi \pm 0.05\pi < 1.54\pi$, and $48.2\ \mu s < 2\pi\tau \pm 16.5\ \mu s < 64.9\ \mu s$. We find these values physically reasonable: Δr provides a reasonable range of radii to account for the change in resistance, and τ is consistent with the speed of switching observed, slow at the start and considerably faster for a small increase in voltage.

4.5.4. Linear and nonlinear contributions to switching dynamics

However, considering the hysteresis curve shown in Figure 27, we see that while the ON state has Ohmic dependence, the OFF state displays strong non-linearity, and the simple geometric modulation of a filament radius cannot account for this linear/non-linear transition. At the nano-scale, the assumption of a perfectly cylindrical filament with constant radius likely fails. As the filament is pinched to a minimum in the OFF state, it is likely that it in fact ruptures and becomes discontinuous due to uneven, inherent surface roughness and non-uniform depletion of oxygen. As a result, the conductive path is below the percolation-threshold, and includes a series insulating component which accounts for the non-linearity. According to this scenario, the static transport equation would contain two parallel conduction contributions from both a perfect cylinder and its discontinuous rough edges such that (calculated from classical geometric resistances):

Equation 11:

$$\boldsymbol{I = V\left[\frac{\pi(r_F - r_{NL})^2}{\rho_{Ta(O)}L} + \frac{\pi(r_F + r_{NL})^2 - \pi r_F^2}{\rho_{NL}(V)L}\right]}$$

where r_{NL} corresponds to an approximate surface roughness of the filament, ρ_{Ta} and ρ_{NL} are the resistivities of Ta and non-linear regions, $\pi(r_F - r_{NL})^2$ represents the area of linear conduction, and $\pi(r_F + r_{NL})^2 - \pi r_F^2$ represents the area of the concentric cylinder of discontinuous non-linear transport. Alternatively, the non-linear region could be interpreted as a portion of the sub-oxide with a sufficiently high conductivity which contributes a parallel (but non-linear) conduction path. However, it is impossible to distinguish these two scenarios, as each would contribute an identical term to Equation 11.

Because the non-perturbative read measurements are made at a single small voltage ($V \approx 1mV$), the curvature associated with the non-linear insulating conduction is not evident. Therefore, to investigate the development of non-linear conduction and complete Equation 11 by specifying the functional form of $\rho_{NL}(V)$, we have performed static IV measurements at set resistance states throughout the continuum between R_{OFF} and R_{ON}. Figure 30 shows IV curves taken at device resistances spaced across the linear to non-linear transition, with the voltage range chosen to limit unintended resistive switching. Non-linearity was determined by calculating the absolute error resulting from linear fits. As seen in the inset of Figure 30 there is a clear crossover from linear conduction at low resistance states to non-linear conduction at high resistance states. Ohmic conduction dominates over the measured voltage range for the majority of the resistance states with non-linear conduction present only at the highest resistances, as expected from our filament radius state variable model. Poole-Frenkel emission, with $\rho_{NL}(V) \propto Ve^{a\sqrt{V}}$, was chosen for the parallel non-linear conduction, and was found to provide the best fits to the data.

In conclusion, we presented a quasi-3D quantitative memristive model which accurately reproduces both ON and OFF switching data in TaO_x over a wide range of device states with the use of a single governing state variable. Counting the ionic flux of individual oxygen ions, we showed that the radius of a Ta rich conducting filament core controls the resistive state of the device, and we derived the associated dynamical memristive state equation as well as its time-dependent solution. Measuring static IV curves across a range of device resistance values we showed that the filament radius model smoothly connects the linear and non-linear conduction regimes. These results are important as this work provides a model capable of quantitatively reproducing dynamic resistive switching data in TaO_x, which may be useful in circuit simulators such as SPICE. Furthermore, while we have tested this model with TaO_x resistive switching data, the results and general physics of the model may be applicable to other binary oxide memristive systems.

4.6. Filament-based memristor device switching model and information storage

4.6.1. Physics model of state switching in filamentary memristors

In collaboration with Dept. 1748, we developed a theoretical model that fits memristive switching data in tantalum oxide-based devices with the use of only three *physical* fitting parameters: the critical activation temperature T_{crit}, thermal conductivity of the device electrodes k_E, and the conductive filament radius r_F. Importantly, the physical fitting parameters were found to all have quite reasonable ranges over our set of test devices: 8.5 nm $< r_{max} <$ 13.2 nm is consistent with the range of previous reports [93], $T_{crit} \approx$ 1300 K -1700 K is in close agreement with finite element thermal modeling [94, 95], and 89 W $m^{-1}K^{-1} < k_E < 120$ W $m^{-1}K^{-1}$ is close to the expected value for the device electrodes used here. The strength of this work lies in the fact that determining filament composition and radius are prohibitively difficult [83, 86] and/or require inaccessible experimental instrumentation [65, 96]. Filament temperature and surrounding thermal resistance - outside of finite element methods such as COMSOL simulations [94, 95] - are not well known experimentally. In contrast, our model provides a complete characterization of the conducting filament algebraically using a single hysteresis curve. We currently have a manuscript prepared on this work that that is under review for publication.

4.6.2. Information storage in filamentary memristor devices

The traditional understanding of memristor devices is that they contain two states – low (ON) and high (OFF) resistance. We have preliminary evidence that traditional approaches to multi-state memory drastically understate the information storage capacity of these devices. Memristor devices require significant Joule heating to become thermally activated, and this activation power can be used as a separate state variable apart from resistance to store information. We demonstrate experimentally, using standard tantalum oxide ReRAM devices, a simple electrical method for storing multiple bits at single resistance values. We also demonstrate that these states can be easily and precisely read electrically to extract the stored data. Currently, we are assembling this work into a publication.

5. NEUROMORPHIC CIRCUIT SIMULATION AND IMPLEMENTATION – SPICE AND XYCE

5.1. Example of a voltage to frequency converter with a memristor element

Voltage to frequency converters (VFCs) take input voltages and convert them into sinusoidal voltage output signals of varying frequency. Therefore, an output frequency may be externally controlled by modulating the input voltage. Simple integrated circuits typically have a single constant voltage power source, which would result in a constant output frequency when applied to a VFC. The typical solution to this problem is to include an on chip assortment (or 'ladder') of reference resistors which may be placed in various series configurations allowing a multiplicity of input voltages into the VFC. Other solutions include laser trimming of resistors in the circuit – a demanding effort that requires an expensive electro-optical hardware setup for precision laser machining. Instead, memristors provide a simpler solution, where a single memristor can have its resistance state changed dynamically and thus supplant the entire 'ladder' of reference resistors. Figure 31 shows a schematic of a printed circuit board for demonstrating a voltage-to-frequency converter with an active memristor element. The figure also demonstrates a SPICE simulation where a single memristor was used to produce a continuous modulation of the output frequency of a generic VFC (for clarity only select frequencies are shown). Currently, we are constructing the printed circuit board to demonstrate this voltage-to-frequency converter with a bread-board incorporation of a MESA fabricated tantalum oxide memristor.

5.2. Implementation of memristor model into Xyce

Based on our recent publications, Dr. Richard Schiek developed a prototyping code to implement in Matlab to ensure the underlying memristor model equations were adequately represented. Initial calculations did not replicate the results presented in the article under preparation [Mickel et al. 2013, Section 4.6.1.]. After consultation, the prototyping code was modified to take into account that the filament radius term in the power equations should be the maximum filament radius and the code duplicated the results presented. With the modeling equations verified, the power - resistance relationship that was proposed (IVon & IVoff) was used to implement a new memristor device in Xyce, Sandia's in-house circuit simulation software package. Equations (2a) and (2b) in the article can be solved for, R, the resistance for this device during the on-switching and off-switching states. Adding in simple ohmic relationships for the behavior during the on and off states will close the set of equations needed. This is encouraging because initial discussions on this topic led us to believe that very-fast time scale heating and diffusion processes within the device would need to be included, thus complicating the model. Our next step will be to implement these equations as a new memristor device in Xyce.

6. CONCLUSIONS

The effort described in this SAND report is multifaceted and spans wet biology work with primary neurons to hardware memory devices fabricated in the MESA facility. The unifying concept that spans this breadth of work is the focus on developing biology-inspired strategies towards computation with future applications to reach exascale levels of computational power. In the first portion of this report, we describe our efforts in wet biology where our initial purpose is to examine optical stimulation of primary neurons. Optical stimulation would provide a strong advantage for interrogating the network architecture of living networks by simultaneous and dynamic stimulation of multiple cells to identify the inputs and outputs of a particular network. Electrical stimulation provides limited stimulation to small numbers of neurons and does not provide dynamic information due to the time needed to move stimulation electrodes to different locations within the network. Chemical stimulation lacks specificity with regard to choosing which neurons to stimulate. Optical stimulation provides 1) specificity, 2) dynamic assessment, and 3) multiple cell interrogation. This work was started with dissociated neurons in culture in order to control as many variables as possible in the experimental setup. We found some evidence for stimulation of neurons directly with light and have shed some insight into the mechanisms by which this occurs.

Our next effort was to improve the biological relevance of our neural preparation by incorporating dissociated neurons into 3D gels. Neurons plated on glass substrates is a simplified preparation useful for early characterization, but a 3D environment comprised of biological proteins is more relevant given the interactions between the living neurons and the 3D substrate and the positive effect these interactions have on *in vitro* neuron maturation. Primary neurons are especially delicate cells, and thus we explored several different gel preparations in order to optimize their long term health and maturity. Positive results were found with silica gels, and future work will focus on the incorporation of neurons into these gels in a microfluidic environment that will permit directed interactions between different neuron cell types.

The first set of efforts described previously (optical stimulation and 3D gel environments for neurons) are largely to prepare the groundwork for experiments focused on studying the information processing in biological tissue networks. Our first set of experiments in mouse brain tissue slices (collaboration with UNM) examined the effect of plasticity (long-term changes in neuron activity) on the frequency filtering properties of corticostriatal networks. We observed that the low-pass properties of the network were modulated by inducing long-term depression and by blocking inhibitory neurotransmitter receptors. In future work, we are interested in incorporating dissociated neurons into 3D gels in a microfluidic device where cortical neurons and striatal neurons are compartmentalized and can be controllably connected together into artificial corticostriatal networks. In this type of preparation, we could then modulate the network architecture and examine the impact on the frequency filtering characteristics and thus information processing, an experiment that is not possible with brain tissue slices where the architecture is fixed and cannot be modulated. In summary, the 1) dissociated neuron preparation, 2) optical stimulation of neurons, 3) incorporation of neurons into 3D gels, and 4) plasticity and frequency filtering studies in brain tissue slices provide a set of tools for examining the role of network architecture on information processing in biological networks.

In the computational portion of this project, our aim was to examine neuromorphic computational systems that display characteristics of biological networks. From our wet biology work, we know that frequency-dependent changes in the state of neurons and/or a population of neurons is one method by which biological networks modulate their information processing capabilities. Also, the ability of neurons to enter/exit multiple states is another method by which biological networks process and store information. In our hardware effort, we examined the use of multiferroic materials due to their ability to hold multiple states in single devices. Memristive devices, which we show are capable of multi-state information processing, were also explored in this project. We developed a set of theoretical models with experimental validation that provide insight into how memristive devices operate, and we fabricate several memristive devices that rely on metallic atom and oxygen vacancy filament-based structures. We are currently exploring the use of memristors to provide dynamic modulation and tuning of a voltage to frequency converter circuit. Future work includes continuing to partner within SNL and with Hewlett Packard to design, fabricate, and characterize memristor devices for implementation into various computational and memory architectures.

7. REFERENCES

[1] R.C. Gonzalez, R.E. Woods, S.L. Eddins, Digital image processing using MATLAB, Gatesmark Publishing Knoxville, 2009.

[2] L.S. Smith, A. Hamilton, Neuromorphic Systems: Engineering Silicon from Neurobiology:[papers at the First European Workshop on Neuromorphic Systems (EWNSI), Held at the University Of Stirling, Scotland, from 29 to 31 August 1997], World Scientific, 1998.

[3] J. Yang, M. Pickett, X. Li, A. OhlbergDouglas, D. Stewart, R. Williams, Nature Nanotechnology, 3 (2008) 429-433.

[4] S.H. Jo, T. Chang, I. Ebong, B.B. Bhadviya, P. Mazumder, W. Lu, Nano Letters, 10 (2010) 1297-1301.

[5] Q. Xia, W. Robinett, M.W. Cumbie, N. Banerjee, T.J. Cardinali, J.J. Yang, W. Wu, X. Li, W.M. Tong, D.B. Strukov, Nano Letters, 9 (2009) 3640-3645.

[6] A.C. Greene, C.M. Washburn, G.D. Bachand, C.D. James, Biomaterials, 32 (2011) 8860-8869.

[7] A. Vogel, J. Noack, G. Hüttman, G. Paltauf, Applied Physics B, 81 (2005) 1015-1047.

[8] D.J. Stevenson, F.J. Gunn-Moore, P. Campbell, K. Dholakia, Journal of the Royal Society Interface, 7 (2010) 863-871.

[9] K. König, Journal of Microscopy, 200 (2000) 83-104.

[10] H. Hirase, V. Nikolenko, J.H. Goldberg, R. Yuste, Journal of neurobiology, 51 (2002) 237-247.

[11] W. Zhou, X.L. Liu, X.H. Lü, J.S. Li, Q.M. Luo, S.Q. Zeng, Chinese Science Bulletin, 53 (2008) 687-694.

[12] J. Ando, N.I. Smith, K. Fujita, S. Kawata, European Biophysics Journal, 38 (2009) 255-262.

[13] H. He, S. Wang, X. Li, S. Li, M. Hu, Y. Cao, C.-Y. Wang, Applied Physics Letters, 100 (2012) 173704-173704-173704.

[14] X. Liu, X. Lv, S. Zeng, W. Zhou, Q. Luo, Applied Physics Letters, 94 (2009) 061113.

[15] N.I. Smith, K. Fujita, T. Kaneko, K. Katoh, O. Nakamura, S. Kawata, T. Takamatsu, Applied Physics Letters, 79 (2001) 1208-1210.

[16] Y. Zhao, Y. Zhang, X. Liu, X. Lv, W. Zhou, Q. Luo, S. Zeng, Optics express, 17 (2009) 1291-1298.

[17] S. Iwanaga, N. Smith, K. Fujita, S. Kawata, Optics express, 14 (2006) 717-725.

[18] M. Lei, H. Xu, H. Yang, B. Yao, Journal of neuroscience methods, 174 (2008) 215-218.

[19] Y. Zhao, X. Liu, W. Zhou, S. Zeng, Applied Physics Letters, 97 (2010) 063703.

[20] S. Iwanaga, T. Kaneko, K. Fujita, N. Smith, O. Nakamura, T. Takamatsu, S. Kawata, Cell biochemistry and biophysics, 45 (2006) 167-176.

[21] A. Uzdensky, V. Savransky, Journal of Photochemistry and Photobiology B: Biology, 39 (1997) 224-228.

[22] N. Nassif, O. Bouvet, M.N. Rager, C. Roux, T. Coradin, J. Livage, Nature Materials, 1 (2002) 42-44.

[23] N. Nassif, C. Roux, T. Coradin, M.-N. Rager, O.M. Bouvet, J. Livage, Journal of Materials Chemistry, 13 (2003) 203-208.

[24] M. Baca, A.M. Allan, L.D. Partridge, M.C. Wilson, Brain research, (2013).

[25] D.A. Jelinek, L.D. Partridge, Neurosci Lett, 530 (2012) 133-137.

[26] A.R. Schiess, C.S. Scullin, L.D. Partridge, The Journal of physiology, 576 (2006) 833-847.

[27] P.R. Mickel, S. Buvaev, A. Kamalov, H. Jeen, P. Finnegan, A. Biswas, A.F. Hebard, C.D. James, Journal of Applied Physics, 114 (2013) 094104.
[28] P.R. Mickel, C.D. James, Eur. Phys. J. Appl. Phys, 62 (2013) 30102.
[29] P.R. Mickel, A.J. Lohn, B.J. Choi, J.J. Yang, M.-X. Zhang, M.J. Marinella, C.D. James, R.S. Williams, Applied Physics Letters, 102 (2013) 223502.
[30] R.E. Cohen, Nature, 358 (1992) 136-138.
[31] N. Setter, D. Damjanovic, L. Eng, G. Fox, S. Gevorgian, S. Hong, A. Kingon, H. Kohlstedt, N.Y. Park, G.B. Stephenson, I. Stolitchnov, A.K. Taganstev, D.V. Taylor, T. Yamada, S. Streiffer, Journal of Applied Physics, 100 (2006) 051606-051606-051646.
[32] S.-Y. Wu, Electron Devices, IEEE Transactions on, 21 (1974) 499-504.
[33] J. Jo, H. Han, J.-G. Yoon, T. Song, S.-H. Kim, T. Noh, Physical Review Letters, 99 (2007) 267602.
[34] I. Stolichnov, A. Tagantsev, N. Setter, J. Cross, M. Tsukada, Applied Physics Letters, 83 (2003) 3362-3364.
[35] A.K. Tagantsev, I. Stolichnov, N. Setter, J.S. Cross, M. Tsukada, Physical Review B, 66 (2002) 214109.
[36] T. Kimura, T. Goto, H. Shintani, K. Ishizaka, T. Arima, Y. Tokura, Nature, 426 (2003) 55-58.
[37] S.-W. Cheong, M. Mostovoy, Nat Mater, 6 (2007) 13-20.
[38] M. Fukunaga, Y. Sakamoto, H. Kimura, Y. Noda, N. Abe, K. Taniguchi, T. Arima, S. Wakimoto, M. Takeda, K. Kakurai, K. Kohn, Physical Review Letters, 103 (2009) 077204.
[39] K.F. Wang, J.M. Liu, Z.F. Ren, Advances in Physics, 58 (2009) 321-448.
[40] A. Hatt, N. Spaldin, The European Physical Journal B, 71 (2009) 435-437.
[41] R. Seshadri, N.A. Hill, Chemistry of materials, 13 (2001) 2892-2899.
[42] Y.-H. Shin, I. Grinberg, I.-W. Chen, A.M. Rappe, Nature, 449 (2007) 881-884.
[43] M. Park, K. No, S. Hong, AIP Advances, 3 (2013) 042114-042114-042116.
[44] R. Nath, S. Hong, J.A. Klug, A. Imre, M.J. Bedzyk, R.S. Katiyar, O. Auciello, Applied Physics Letters, 96 (2010) 163101-163101-163103.
[45] M. Park, S. Hong, J.A. Klug, M.J. Bedzyk, O. Auciello, K. No, A. Petford-Long, Applied Physics Letters, 97 (2010) 112907.
[46] T. Jungk, A. Hoffmann, M. Fiebig, E. Soergel, Applied Physics Letters, 97 (2010) 012904-012903.
[47] S. Elisabeth, Journal of Physics D: Applied Physics, 44 (2011) 464003.
[48] H. Jeen, G. Singh-Bhalla, P.R. Mickel, K. Voigt, C. Morien, S. Tongay, A.F. Hebard, A. Biswas, Journal of Applied Physics, 109 (2011) 074104-074105.
[49] R. Igreja, C.J. Dias, Sensors and Actuators A: Physical, 112 (2004) 291-301.
[50] Y. Chen, J. Washburn, Physical Review Letters, 77 (1996) 4046-4049.
[51] Q. Liu, S. Long, H. Lv, W. Wang, J. Niu, Z. Huo, J. Chen, M. Liu, ACS Nano, 4 (2010) 6162-6168.
[52] R. Waser, M. Aono, Nat Mater, 6 (2007) 833-840.
[53] H.P. Wong, S. Raoux, S. Kim, J. Liang, J.P. Reifenberg, B. Rajendran, M. Asheghi, K.E. Goodson, Proceedings of the IEEE, 98 (2010) 2201-2227.
[54] A. Ramirez, Journal of Physics: Condensed Matter, 9 (1997) 8171.
[55] G.W. Burr, B.N. Kurdi, J.C. Scott, C.H. Lam, K. Gopalakrishnan, R.S. Shenoy, IBM Journal of Research and Development, 52 (2008) 449-464.
[56] R. Waser, R. Dittmann, G. Staikov, K. Szot, Advanced Materials, 21 (2009) 2632-2663.

[57] T. Hickmott, Journal of Applied Physics, 33 (1962) 2669-2682.
[58] J.F. Gibbons, W.E. Beadle, Solid-State Electronics, 7 (1964) 785-790.
[59] D. Strukov, G. Snider, D. Stewart, R. Williams, Nature, 453 (2008) 80-83.
[60] L.O. Chua, K. Sung Mo, Proceedings of the IEEE, 64 (1976) 209-223.
[61] L. Chua, Circuit Theory, IEEE Transactions on, 18 (1971) 507-519.
[62] T. Chang, S.-H. Jo, W. Lu, ACS Nano, 5 (2011) 7669-7676.
[63] G.S. Snider, Spike-timing-dependent learning in memristive nanodevices, in: Nanoscale Architectures, 2008. NANOARCH 2008. IEEE International Symposium on, 2008, pp. 85-92.
[64] Y.V. Pershin, M. Di Ventra, Proceedings of the IEEE, 100 (2012) 2071-2080.
[65] D.-H. Kwon, K.M. Kim, J.H. Jang, J.M. Jeon, M.H. Lee, G.H. Kim, X.-S. Li, G.-S. Park, B. Lee, S. Han, M. Kim, C.S. Hwang, Nat Nano, 5 (2010) 148-153.
[66] J.J. Yang, M.D. Pickett, X. Li, A.A. OhlbergDouglas, D.R. Stewart, R.S. Williams, Nat Nano, 3 (2008) 429-433.
[67] Y.C. Yang, F. Pan, Q. Liu, M. Liu, F. Zeng, Nano Letters, 9 (2009) 1636-1643.
[68] H. Tanaka, K. Kinoshita, M. Yoshihara, S. Kishida, AIP Advances, 2 (2012) 022141-022141-022146.
[69] P. Sheridan, K.-H. Kim, S. Gaba, T. Chang, L. Chen, W. Lu, Nanoscale, 3 (2011) 3833-3840.
[70] U. Russo, D. Kamalanathan, D. Ielmini, A.L. Lacaita, M.N. Kozicki, Electron Devices, IEEE Transactions on, 56 (2009) 1040-1047.
[71] D. Strukov, R. Williams, Applied Physics A: Materials Science & Processing, 94 (2009) 515-519.
[72] N. Dimin, C. Yiran, X. Cong, X. Yuan, Impact of process variations on emerging memristor, in: Design Automation Conference (DAC), 2010 47th ACM/IEEE, 2010, pp. 877-882.
[73] H. Jing, M.B. Tahoori, F. Lombardi, On the defect tolerance of nano-scale two-dimensional crossbars, in: Defect and Fault Tolerance in VLSI Systems, 2004. DFT 2004. Proceedings. 19th IEEE International Symposium on, 2004, pp. 96-104.
[74] M. Di Ventra, Y.V. Pershin, L.O. Chua, Proceedings of the IEEE, 97 (2009) 1717-1724.
[75] M. Krems, Y.V. Pershin, M. Di Ventra, Nano Letters, 10 (2010) 2674-2678.
[76] J. Martinez-Rincon, M. Di Ventra, Y.V. Pershin, Physical Review B, 81 (2010) 195430.
[77] Y.V. Pershin, M. Di Ventra, Advances in Physics, 60 (2011) 145-227.
[78] T. Driscoll, H.-T. Kim, B.-G. Chae, B.-J. Kim, Y.-W. Lee, N.M. Jokerst, S. Palit, D.R. Smith, M. Di Ventra, D.N. Basov, Science, 325 (2009) 1518-1521.
[79] D.B. Strukov, G.S. Snider, D.R. Stewart, R.S. Williams, Nature, 453 (2008) 80-83.
[80] D.B. Strukov, J.L. Borghetti, R.S. Williams, Small, 5 (2009) 1058-1063.
[81] J. Borghetti, G.S. Snider, P.J. Kuekes, J.J. Yang, D.R. Stewart, R.S. Williams, Nature, 464 (2010) 873-876.
[82] M.-J. Lee, C.B. Lee, D. Lee, S.R. Lee, M. Chang, J.H. Hur, Y.-B. Kim, C.-J. Kim, D.H. Seo, S. Seo, U.I. Chung, I.-K. Yoo, K. Kim, Nat Mater, 10 (2011) 625-630.
[83] F. Miao, J.P. Strachan, J.J. Yang, M.-X. Zhang, I. Goldfarb, A.C. Torrezan, P. Eschbach, R.D. Kelley, G. Medeiros-Ribeiro, R.S. Williams, Advanced Materials, 23 (2011) 5633-5640.
[84] J.J. Yang, M.X. Zhang, J.P. Strachan, F. Miao, M.D. Pickett, R.D. Kelley, G. Medeiros-Ribeiro, R.S. Williams, Applied Physics Letters, 97 (2010) 232102-232103.
[85] J.H. Hur, M.-J. Lee, C.B. Lee, Y.-B. Kim, C.-J. Kim, Physical Review B, 82 (2010) 155321.

[86] F. Miao, W. Yi, I. Goldfarb, J.J. Yang, M.-X. Zhang, M.D. Pickett, J.P. Strachan, G. Medeiros-Ribeiro, R.S. Williams, ACS Nano, 6 (2012) 2312-2318.
[87] Z. Wei, T. Takagi, Y. Kanzawa, Y. Katoh, T. Ninomiya, K. Kawai, S. Muraoka, S. Mitani, K. Katayama, S. Fujii, Demonstration of high-density ReRAM ensuring 10-year retention at 85 C based on a newly developed reliability model, in: Electron Devices Meeting (IEDM), 2011 IEEE International, IEEE, 2011, pp. 31.34. 31-31.34. 34.
[88] J.J. Yang, D.B. Strukov, D.R. Stewart, Nat Nano, 8 (2013) 13-24.
[89] D. Strukov, F. Alibart, R. Stanley Williams, Appl. Phys. A, 107 (2012) 509-518.
[90] S. Duhr, D. Braun, Proceedings of the National Academy of Sciences, 103 (2006) 19678-19682.
[91] J. Janek, H. Timm, Journal of Nuclear Materials, 255 (1998) 116-127.
[92] M.D. Pickett, D.B. Strukov, J.L. Borghetti, J.J. Yang, G.S. Snider, D.R. Stewart, R.S. Williams, Journal of Applied Physics, 106 (2009) 074508-074506.
[93] F. Miao, W. Yi, I. Goldfarb, J.J. Yang, M.-X. Zhang, M.D. Pickett, J.P. Strachan, G. Medeiros-Ribeiro, R.S. Williams, ACS Nano, 6 (2012) 2312-2318.
[94] S. Larentis, C. Cagli, F. Nardi, D. Ielmini, Microelectronic Engineering, 88 (2011) 1119-1123.
[95] D.B. Strukov, F. Alibart, R.S. Williams, Applied Physics A, 107 (2012) 509-518.
[96] M.-J. Lee, C.B. Lee, D. Lee, S.R. Lee, M. Chang, J.H. Hur, Y.-B. Kim, C.-J. Kim, D.H. Seo, S. Seo, Nature materials, 10 (2011) 625-630.

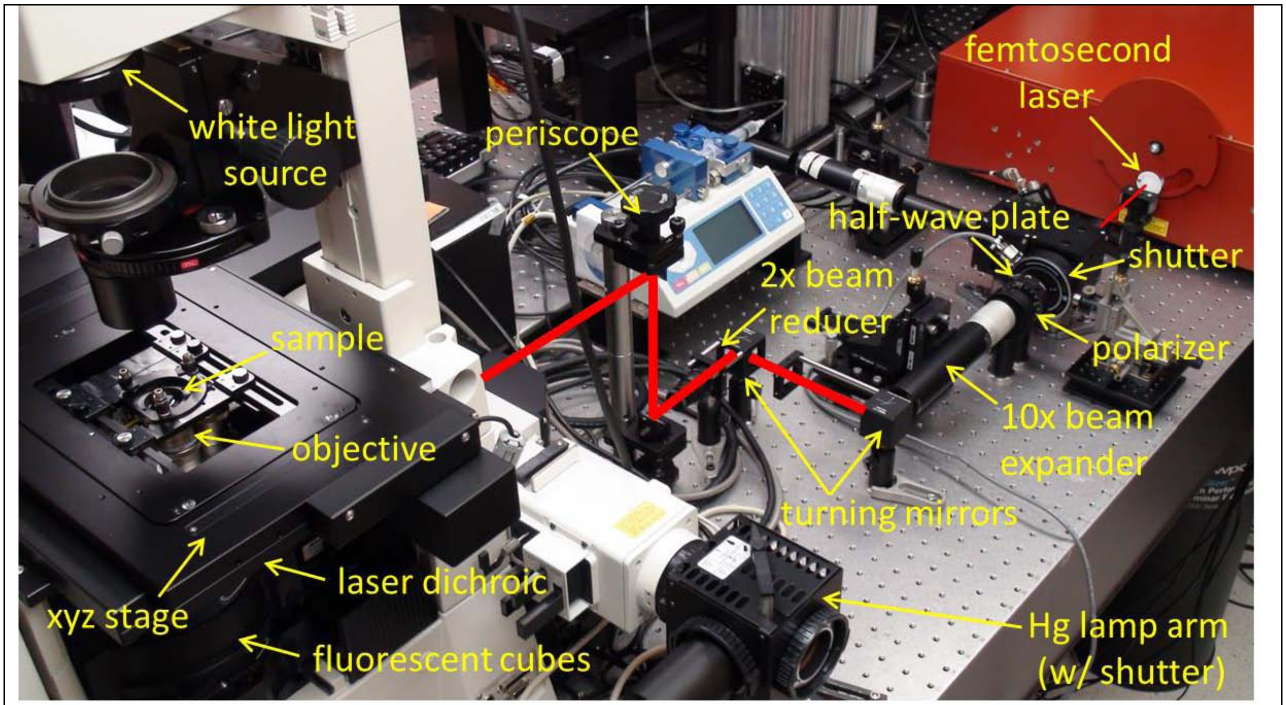
femtosecond laser
white light source
periscope
half-wave plate
shutter
2x beam reducer
polarizer
sample
10x beam expander
objective
turning mirrors
laser dichroic
xyz stage
Hg lamp arm (w/ shutter)
fluorescent cubes

Figure 1: Experimental setup for femtosecond laser stimulation and epifluorescence imaging of neurons.

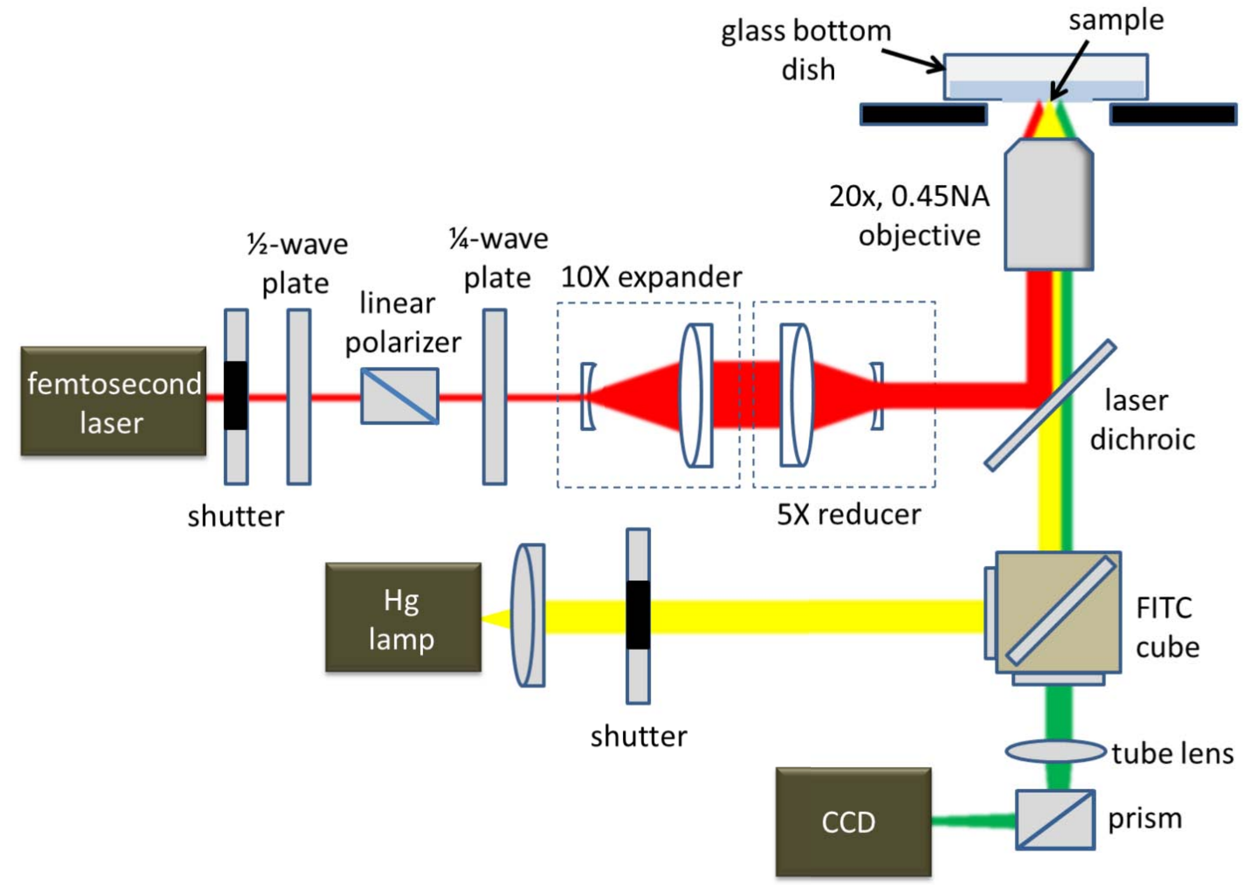
glass bottom dish
sample
20x, 0.45NA objective
½-wave plate
¼-wave plate
linear polarizer
10X expander
femtosecond laser
laser dichroic
shutter
5X reducer
Hg lamp
FITC cube
shutter
tube lens
CCD
prism

Figure 2: Schematic of the optical setup for femtosecond laser stimulation and epifluorescence imaging of neurons.

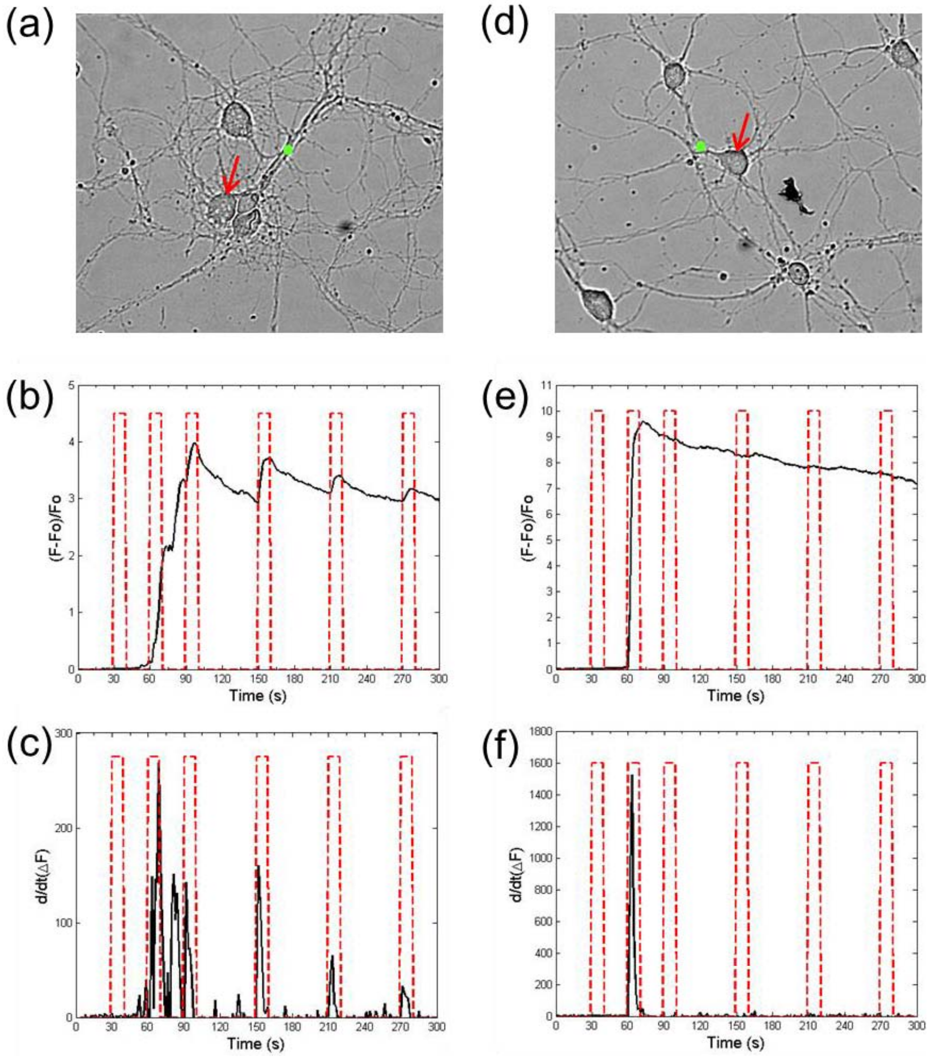

Figure 3: Fluorescence response of neurons optically stimulated at 75mW average power (a-c) and at 160mW average power (d-f). (a) Brightfield image of a neural network showing the location of the focal spot (circle) and the cell body of interest (arrow). (b) Normalized intensity versus time calculated from the average fluorescence across the soma when exposed to 6 sets of optical irradiations (dashed lines). (c) Time derivative of the fluorescence showing the relatively intensity change between successive frames in the sequence. (d-f) Corresponding image and plots from a different sample at 160mW.

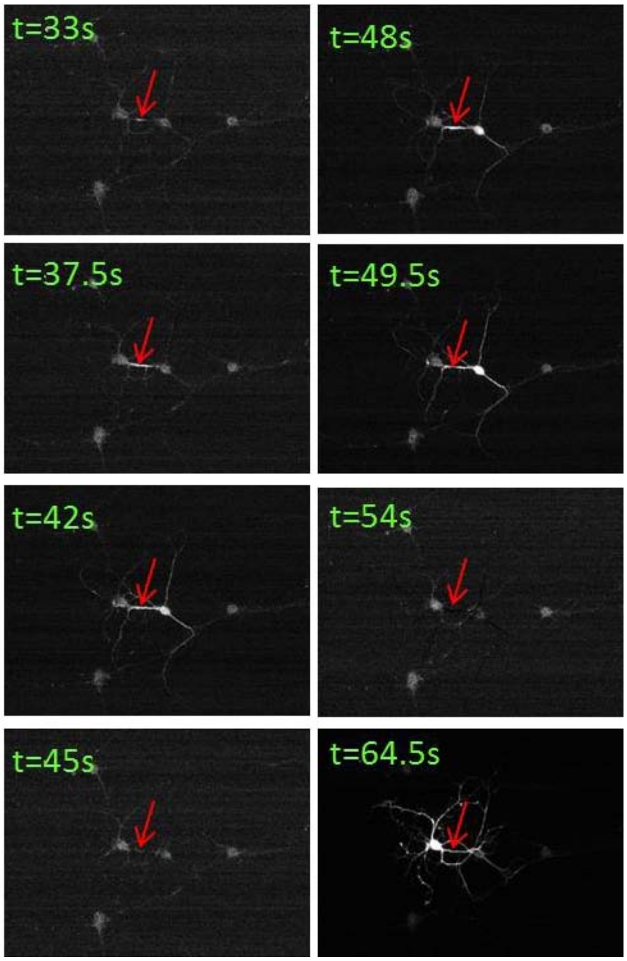
t=33s
t=48s
t=37.5s
t=49.5s
t=42s
t=54s
t=45s
t=64.5s

Figure 4: Differential fluorescence images of Ca^{2+} concentration after laser stimulation. The arrow denotes the laser stimulation location.

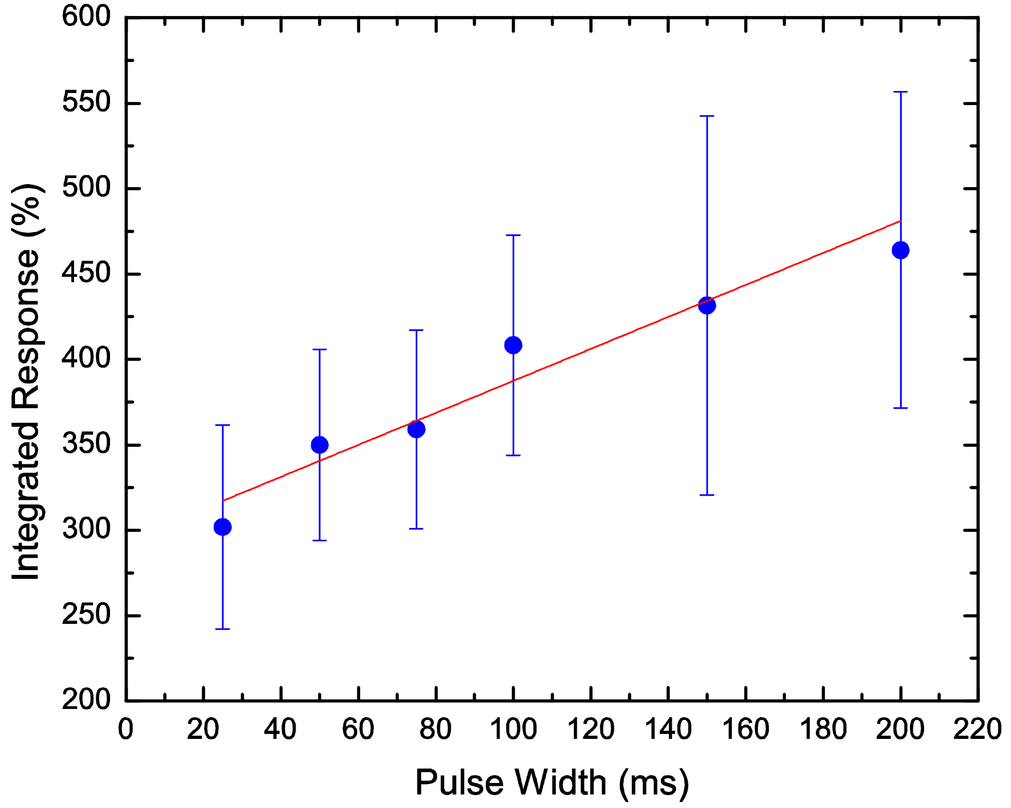

Figure 5: Variation of fluorescence response with laser pulse width. A linear fit to the data is also shown.

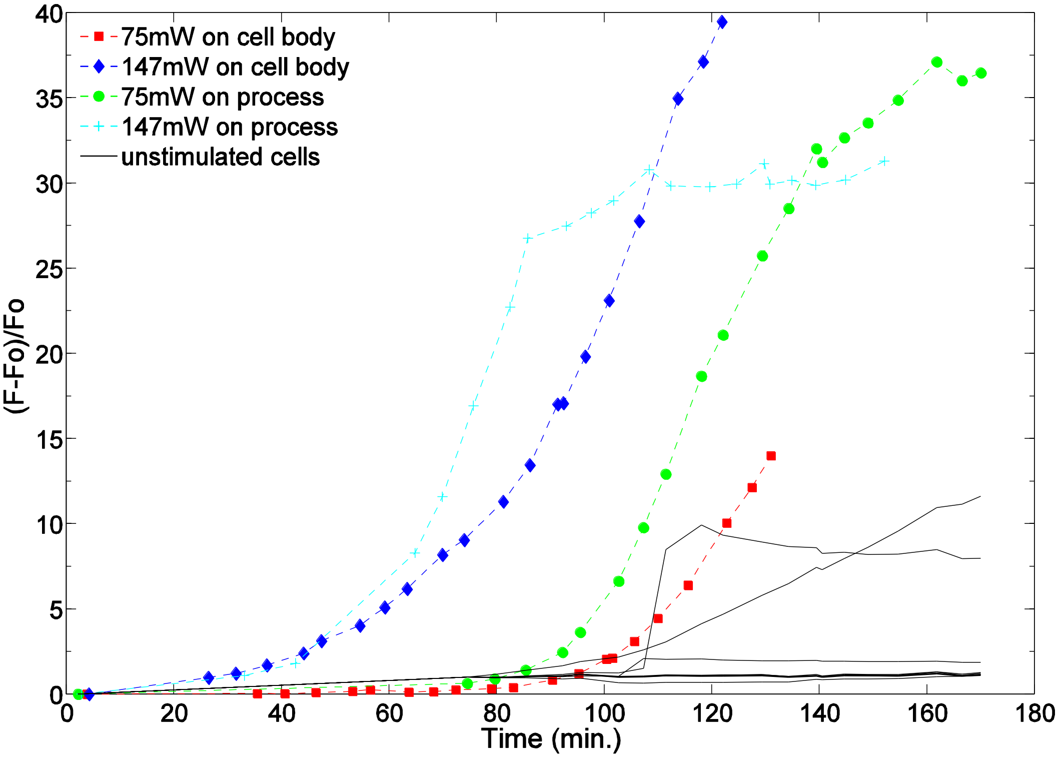

Figure 6: Red channel fluorescence over time for a solution with 20µM of propidium iodide (PI) added to the extracellular matrix. Several nearby cells in the field of view that were not directly stimulated are also shown.

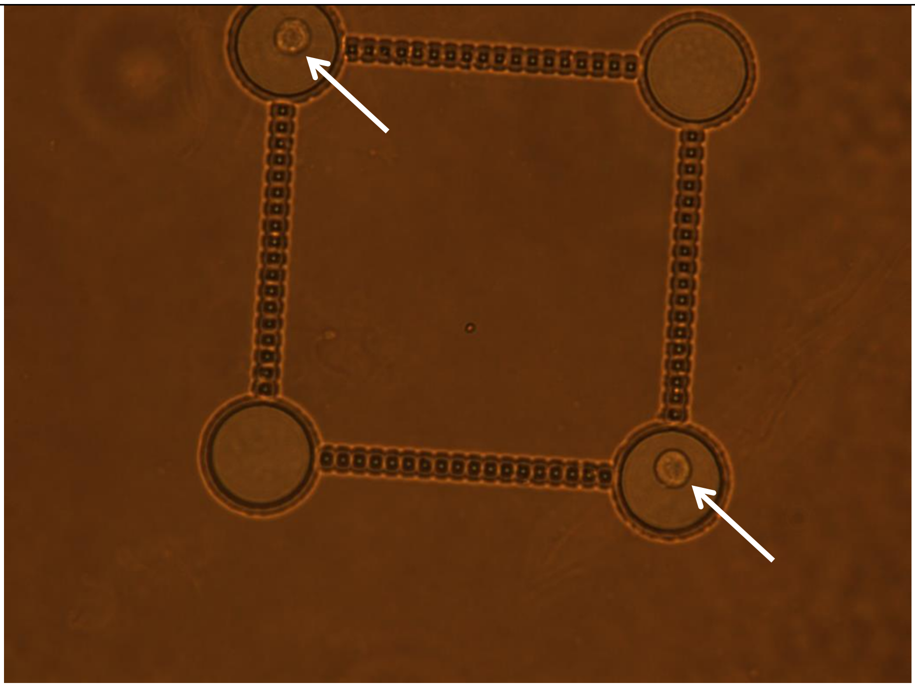

Figure 7: Image of two neurons (arrows) placed into guidance cue nodes with laser tweezers on day 1 in culture.

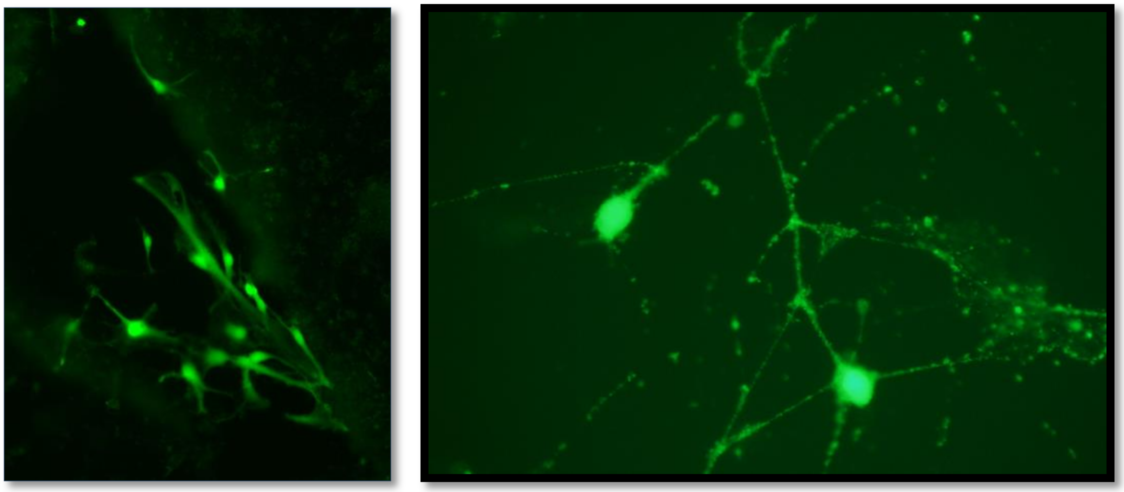

Figure 8: (left) Sodium silicate derived matrix encapsulated 7 days. (right) Poly(glycerol) silicate derived matrix containing Neuro-basal medium (encapsulated 7 Days).

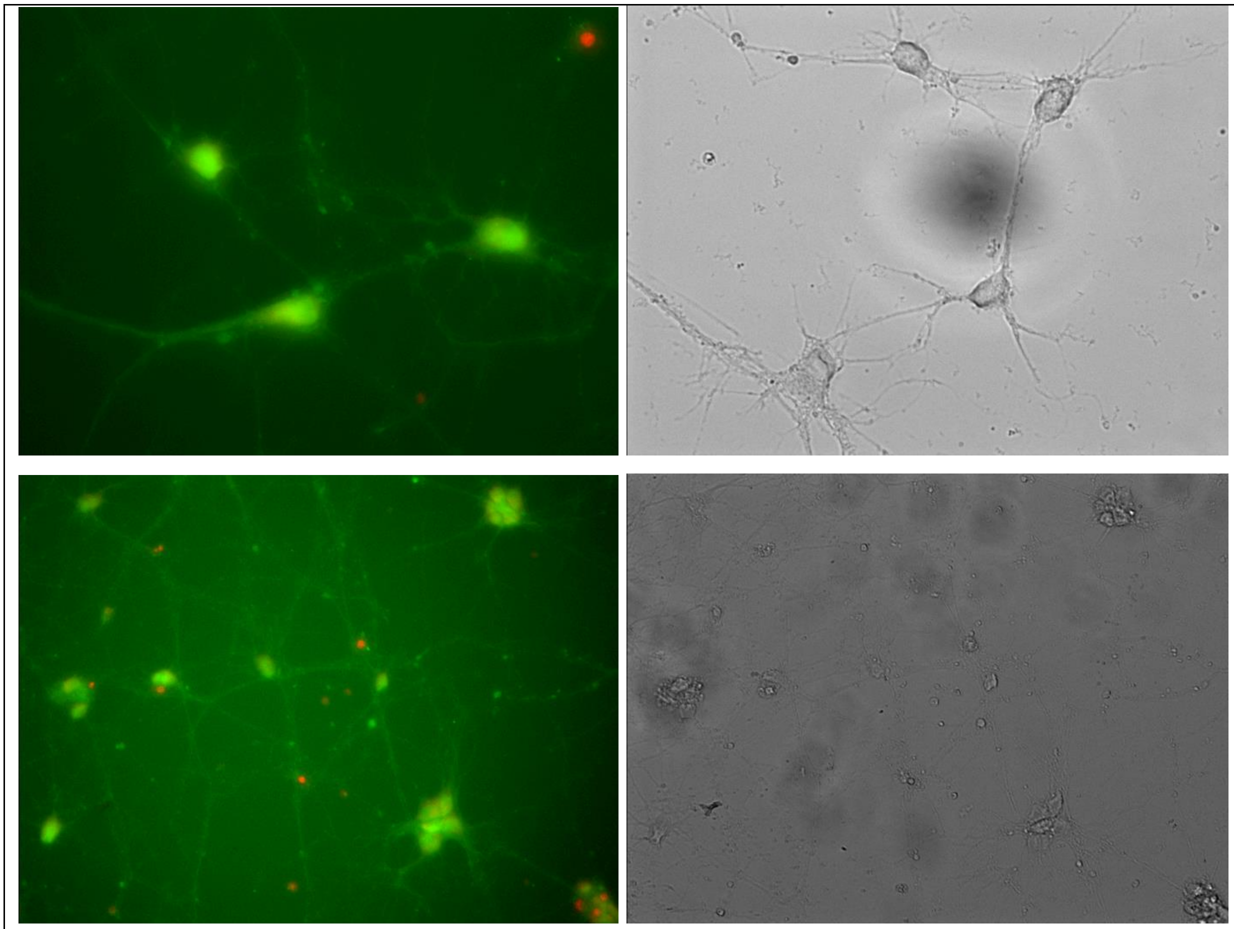

Figure 9: (top) Poly(glycerol) Silicate-derived matrix containing Neuro-basal medium and 1.5 mg/mL collagen (encapsulated 7 days). (bottom) Poly(glycerol) silicate derived matrix containing Neuro-basal medium and 2.5 mg/mL collagen (encapsulated 7 days).

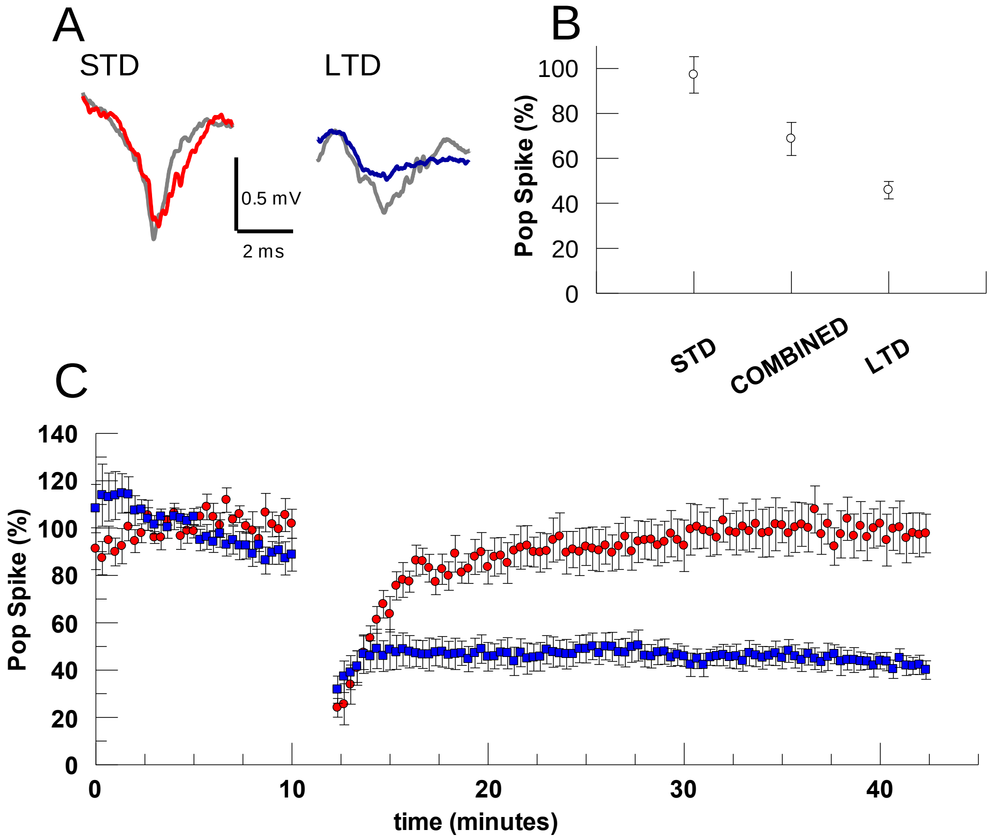

Figure 10: A) Representative example of fEPSP population spikes before (gray) and after (red, blue) 4 x 10 Hz maximum HFS paradigm from STD cluster (> 70% recovery, n = 8, red) and LTD cluster (<60% recovery, n = 10, blue). B) Mean +/- SEM of individual LTD and STD clusters and combined data for test population spike amplitudes shown in C. C) Time course of normalized population spike amplitudes separated into 2 groups determined by cluster analysis of amplitudes during test period (30 min after HFS).

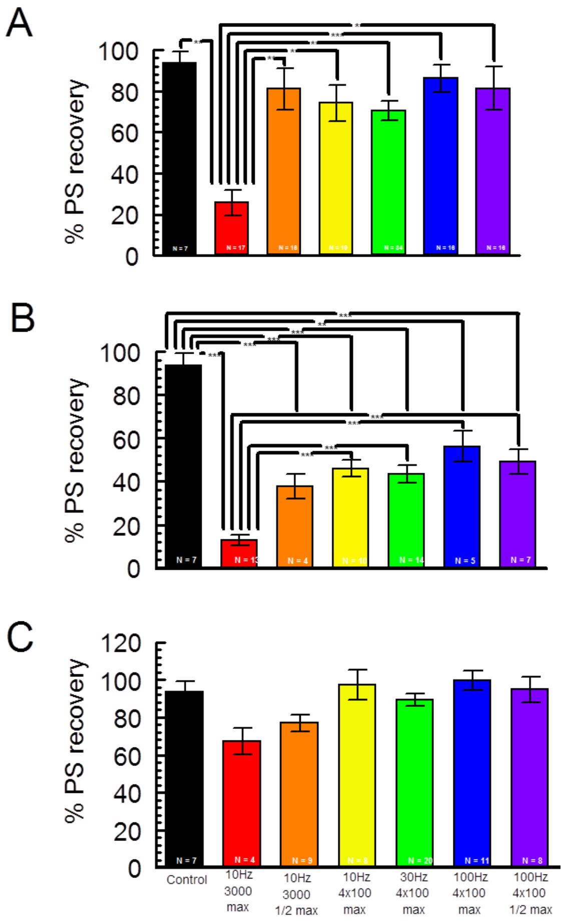

Figure 11: A) Percent recovery of population spike amplitudes before cluster analysis. Statistics: ANOVA multiple comparisons mean squares between groups = 7590.7, mean squares within groups = 1058.9, F = 7.1687, *p* < 0.0001with Scheffe's posthoc. B) Percent recovery of population spike amplitude for clusters with the weakest recovery. Statistics: ANOVA multiple comparisons, mean squares between groups = 5135.8 F=28.5296, *p* < 0.0001, with Scheffe's posthoc C) Percent recovery of population spike amplitude for clusters with the strongest recovery. Statistics: ANOVA multiple comparisons mean squares between groups = 883.3, F= 3.0877, *p* = 0.016, Scheffe's posthoc – no significant differences.

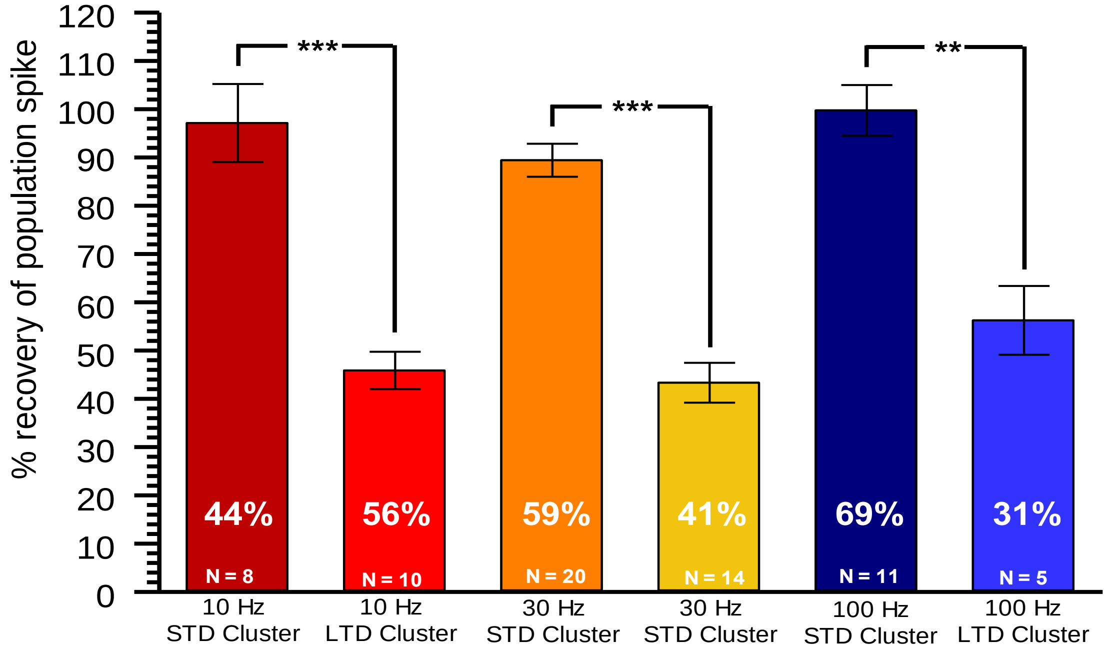

Figure 12: Clusters with 4 x 100 stimuli at max I_{stim}. Percent recovery of population spike amplitude for all clusters with a HFS paradigm with 4 x 100 stimuli at maximum I_{stim}. Statistics: ANOVA multiple comparisons, 2 × 3, mean squares between groups = 7790.4, F = 29.2047, *p* < 0.0001, with Scheffe's posthoc.

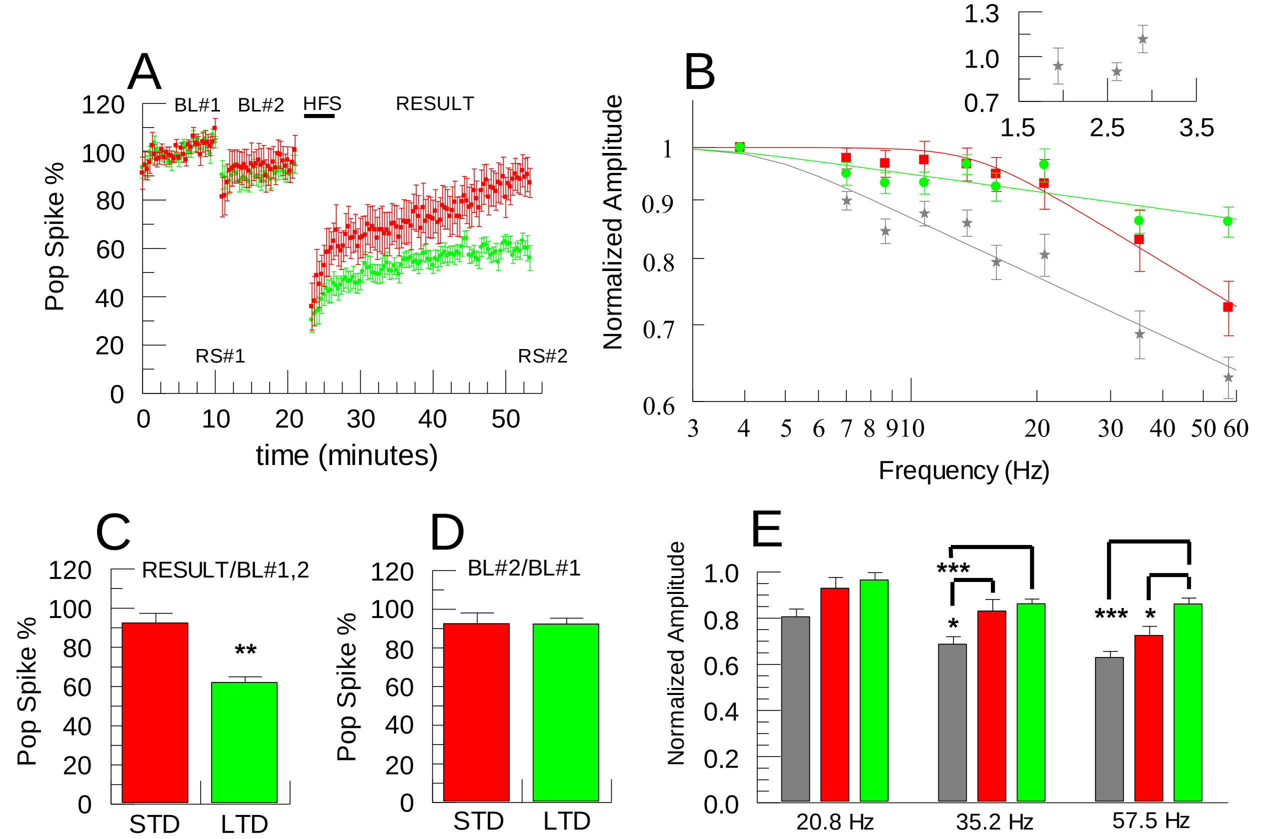

Figure 13: Effect of long-term plasticity on filtering for 10 Hz, 400 stimuli at maximum intensity HFS paradigm. A) Time course of normalized population spike amplitudes separated into 2 groups (STD and LTD). B) Low pass filter properties for 10 Hz, 400 stimuli at maximum intensity. 3rd order Butterworth low pass filter fits to random frequency stimuli either before or after 10 Hz HFS paradigm. Clusters (RS# 1 (grey), COF = 4.3688 Hz, A=0.0185, n=22; RS# 2 STD cluster (red): COF = 14.2026 Hz, A = 0.0370; n = 7; RS# 2 LTD cluster (green): COF = 3.4474, A=0.0084; n=15). Inset shows averages of the lowest 3 frequencies used in random stimulus paradigm (n=6). C) Bar graph of STD (mean 92.50 +/- 4.87, red) and LTD (62.11 +/- 2.78, green) clusters of results 30 minutes after HFS from time course plots in A. D) Bar graph of ratio of 10 minute BL#1 to BL#2 for STD and LTD clusters. E) Comparison of RS# 1 (grey), RS# 2 STD cluster (red), and RS# 2 LTD cluster (green) frequency responses at 20.8 Hz, 35.2 Hz and 57.5 Hz.

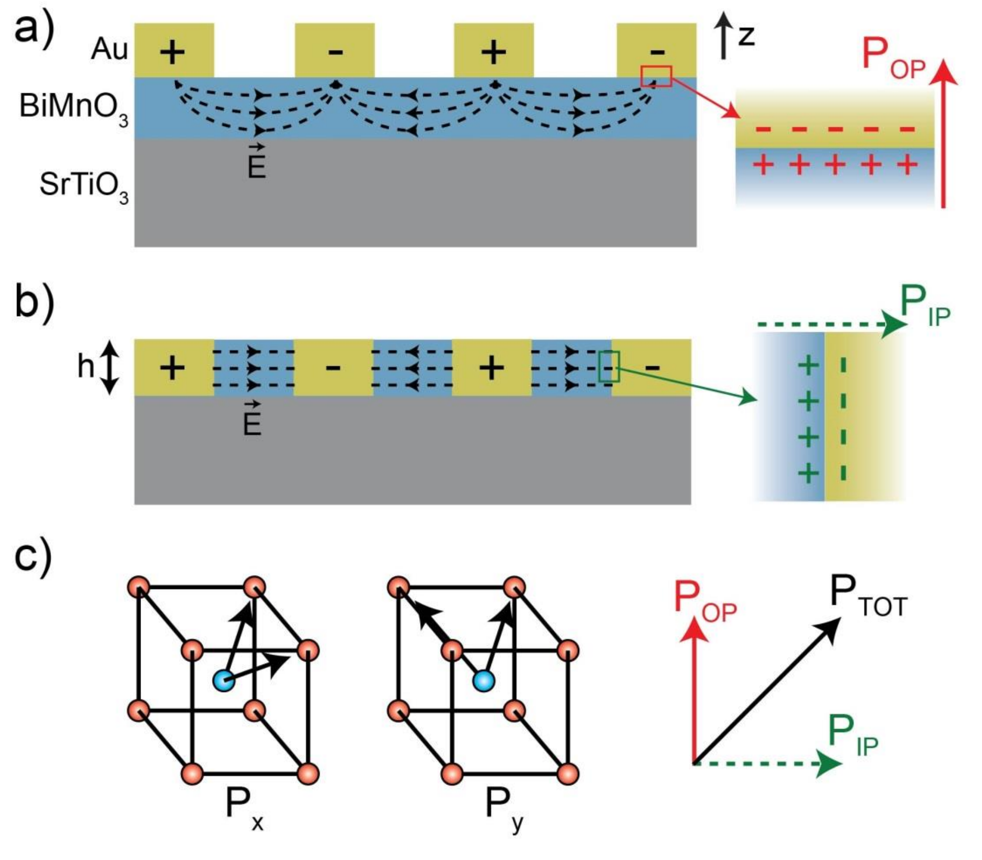

Figure 14: (a) Surface interdigital microelectrode device configuration for a bismuth manganite ($BiMnO_3$, BMO) multiferroic thin film. Gold microelectrodes (Au) and the strontium titanate ($SrTiO_3$, STO) substrate are shown. Electric field lines ($\vec{E}$) when voltage is applied across the microelectrodes and the subsequent induced bound charge out-of-plane polarization (P_{OP}) at the BMO/metal interface are also shown. (b) Embedded interdigital microelectrode device configuration for measuring in-plane ferroelectric properties. The in-plane (P_{IP}), out-of-plane (P_{OP}), and total vector polarization (P_{TOT}) are shown. (c) Degenerate ferroelectric polarization vectors corresponding to electric fields applied along the x and y axes of a ferroelectric film are shown. The total polarization vector (P_{TOT}) is also shown as a combination of the in-plane and out-of-plane polarization vectors.

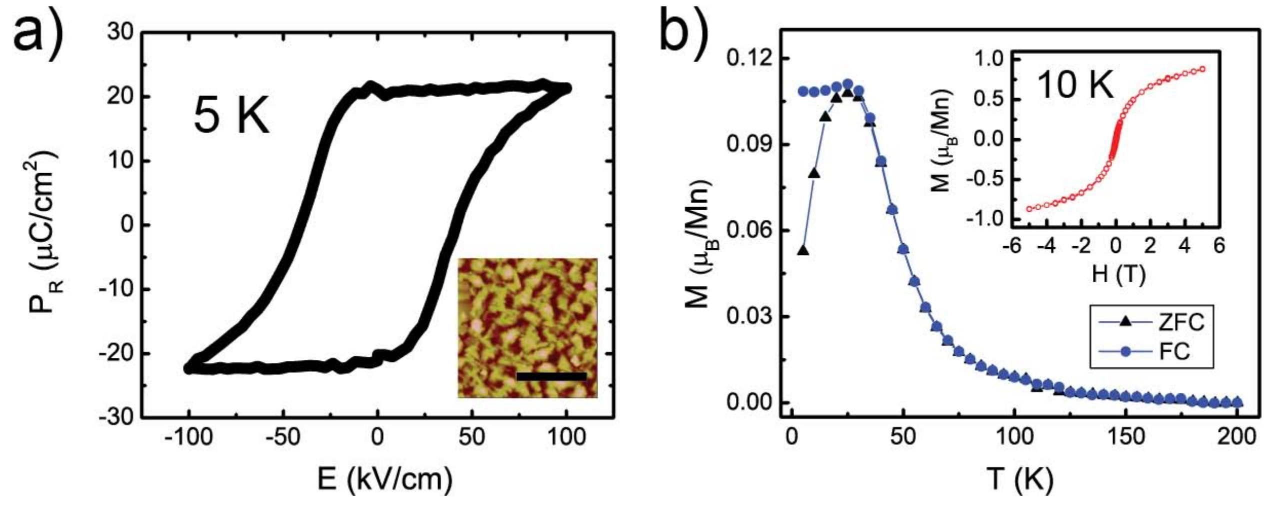

Figure 15: a) Remanent ferroelectric polarization measured at 5 K via surface interdigital microelectrodes. Inset: AFM image of film morphology. b) Zero-field-cooled and field-cooled magnetization measured in a magnetic field of 1000 Oe is shown. Inset: magnetization vs. magnetic field hysteresis shows strong non-linearity and quasi saturation.

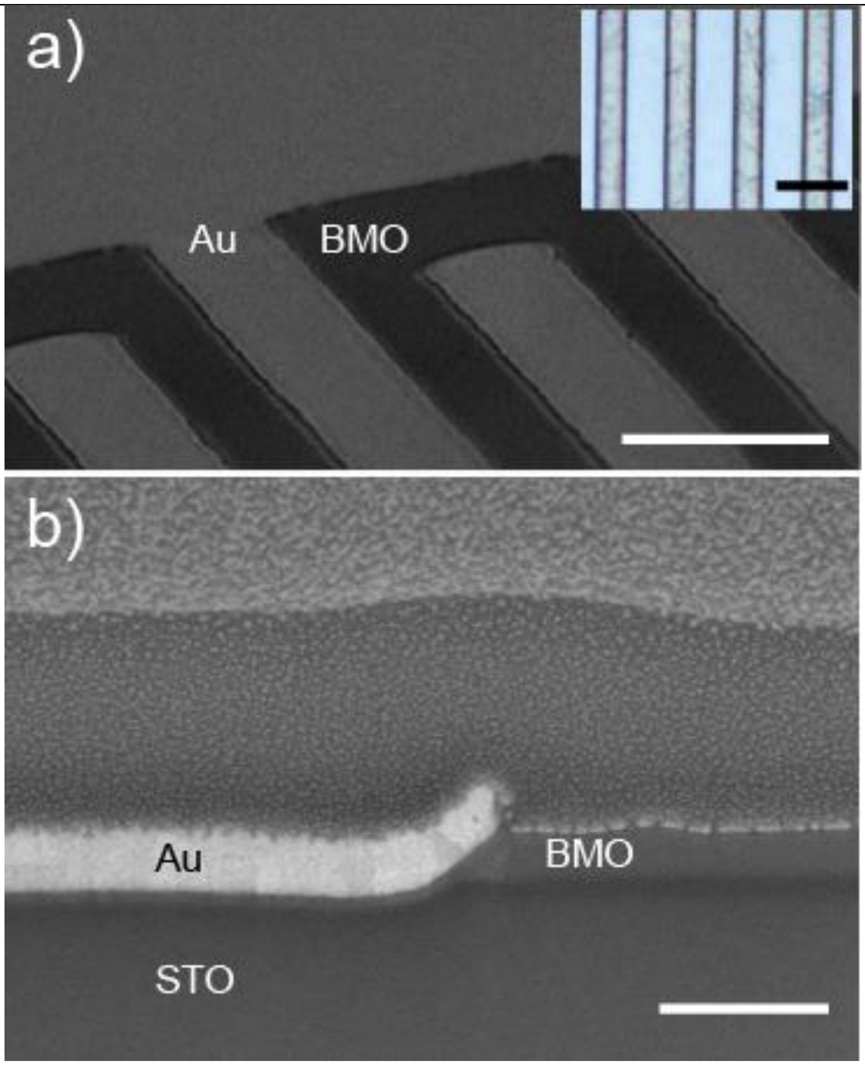

Figure 16:(a) Scanning electron microscope image of an embedded interdigital microelectrode array device. Bright-field image (inset). Scale bars = 10 µm. (b) Cross-sectional image of an embedded interdigital microelectrode array device (coated with two layers of Pt for milling/imaging). Scale bar = 200 nm.

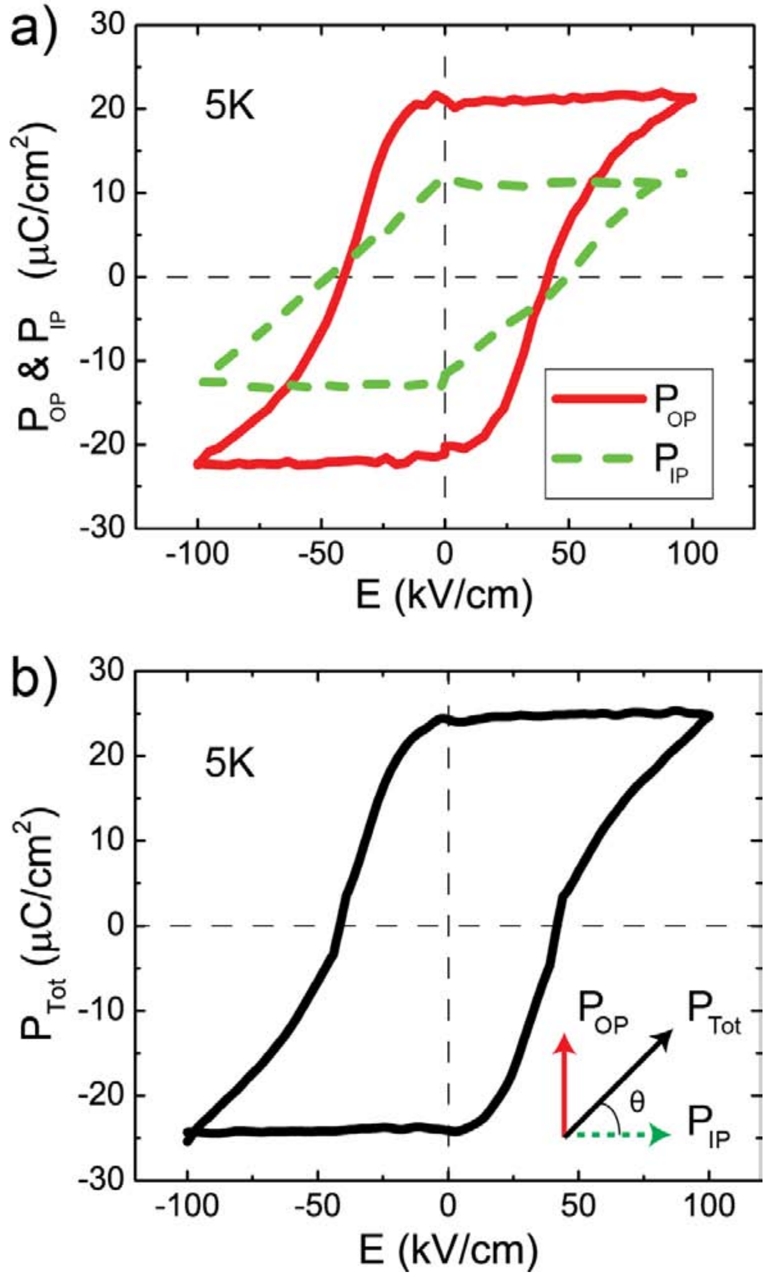

Figure 17: (a) The out-of-plane (solid red line) and in-plane (dashed green line) remanent polarizations are shown for the surface and embedded interdigital electrodes, respectively, taken at 5 K. (b) The calculated total remanent polarization magnitude, P_{Tot}, inferred from P_{OP} and P_{IP}.

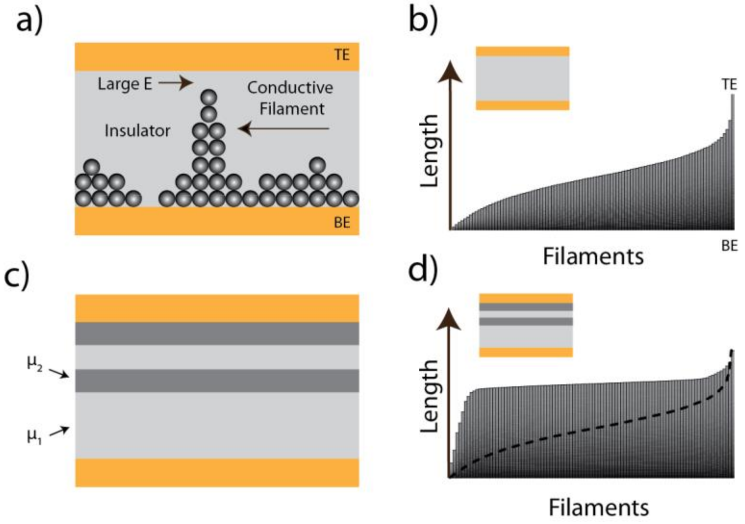
a)
TE
Large E
Conductive Filament
Insulator
BE
b)
Length
TE
Filaments
BE
c)
μ_2
μ_1
d)
Length
Filaments

Figure 18: (a) Schematic of a conventional memristive device with an insulator layer sandwiched by a top (TE) and bottom electrode (BE). Conductive filaments made of mobile carriers grow under an electric field between the electrodes. (b) Simulation of the filament length distribution (n=100 filaments) in a single layer device. Filament lengths are sorted in ascending order for clarity. (c) A memristive device structure with multiple layers of alternating ionic mobility (μ_1, μ_2). (d) Simulation of the filament length distribution in the multi-layered device structure demonstrates larger average lengths with more uniformity than the distribution of the single layer device shown in panel b (dashed black line).

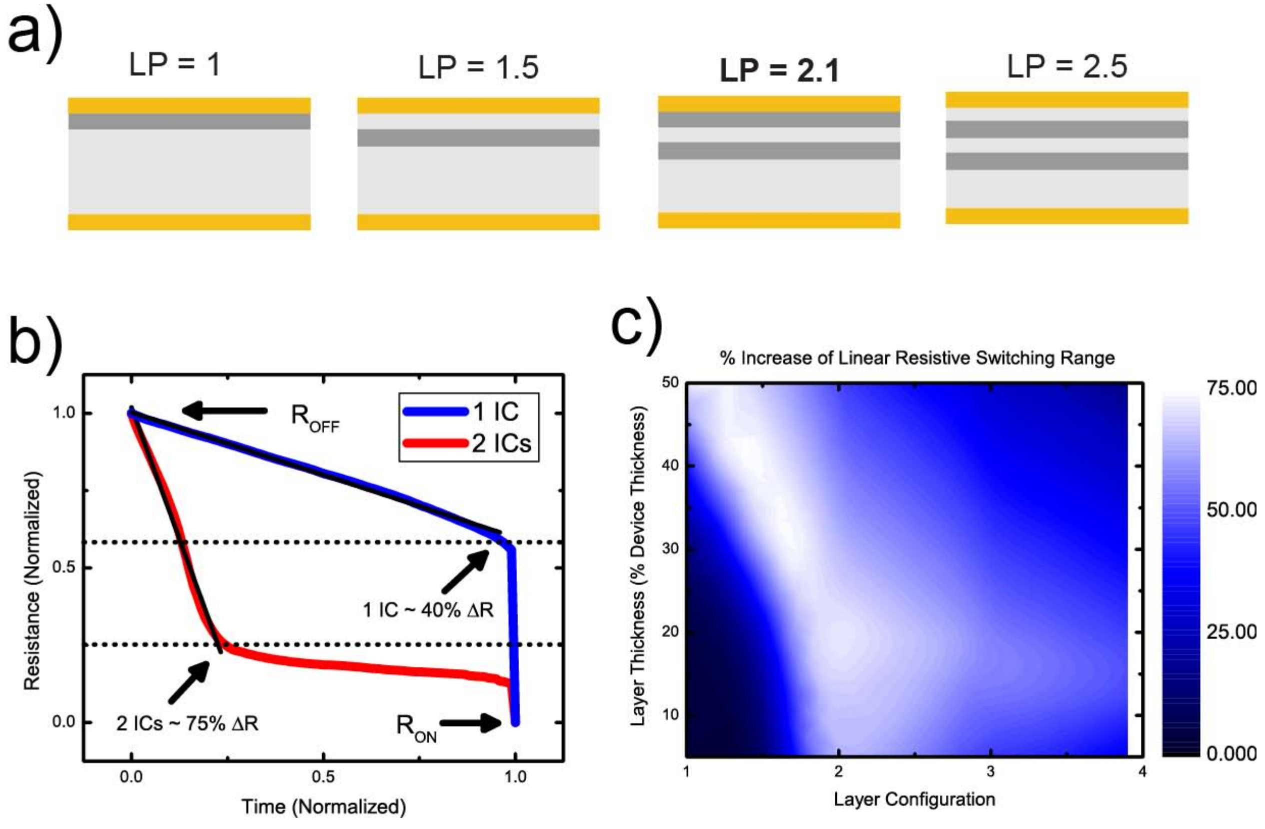

Figure 19: (a) Schematic of the phase-space coordinate layer-configuration (LC, see text), LC = 1.6 (bolded) was used for the switching profile shown in Fig. 2b. (b) The range of linear resistance modulation is shown to be as much as 75% ΔR in the memristor structure with two ionic conductors (IC, red), a 75% increase compared to a conventional single ionic conductor memristor structure with ~ 44% ΔR (blue). The resistance curves are normalized by their OFF state resistances, which are calculated as: $R_{off}=(\sum \rho_n L_n)/A$ where ρ_n is the resistivity of each ionic conductor layer, L_n is the total thickness of all layers of that ionic conductor, and A is the area of the memristor structure. (c) Plot of the optimized design phase space for the increase in the range of linear resistive switching as a function of layer thickness and configuration.

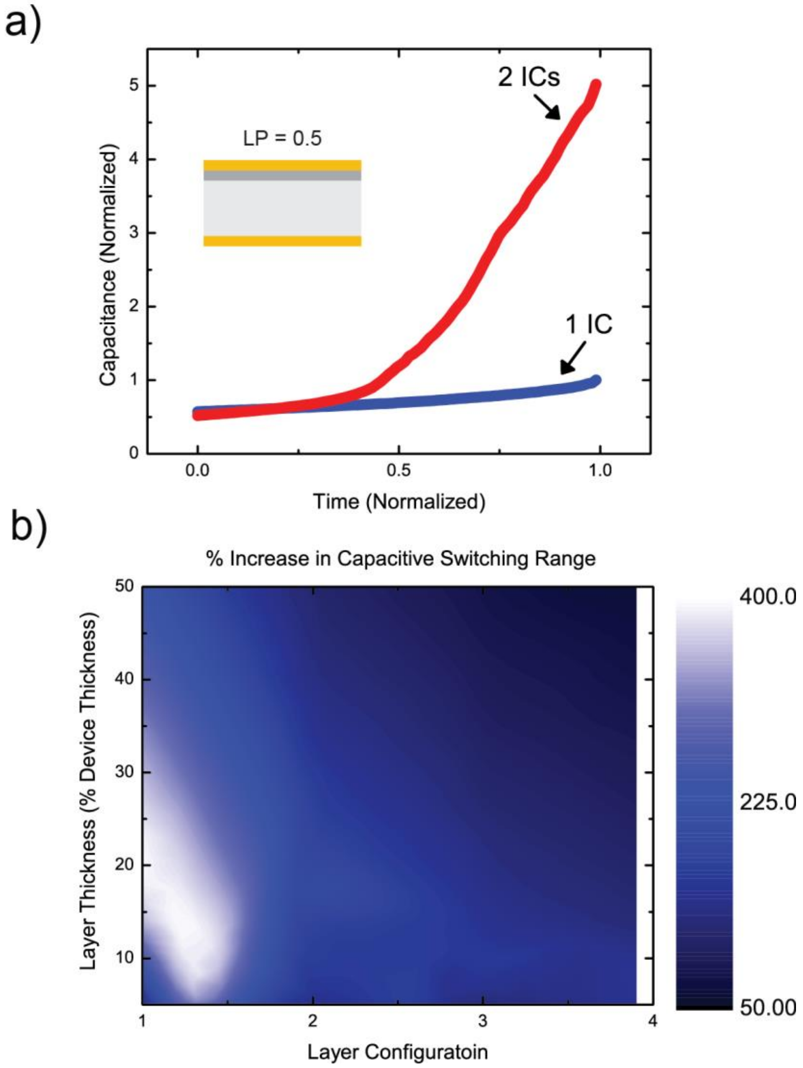

Figure 20: (a) The capacitance switching of a conventional single layer memristor (1 IC, blue) and an alternating ionic conductor memristor (2 ICs, red) are compared. Inset: The device design for the capacitive switching behavior for Fig. 3a is shown. (b) The design space spanned by layer-thickness and layer-configuration is shown for capacitive switching, identifying optimal device design parameters.

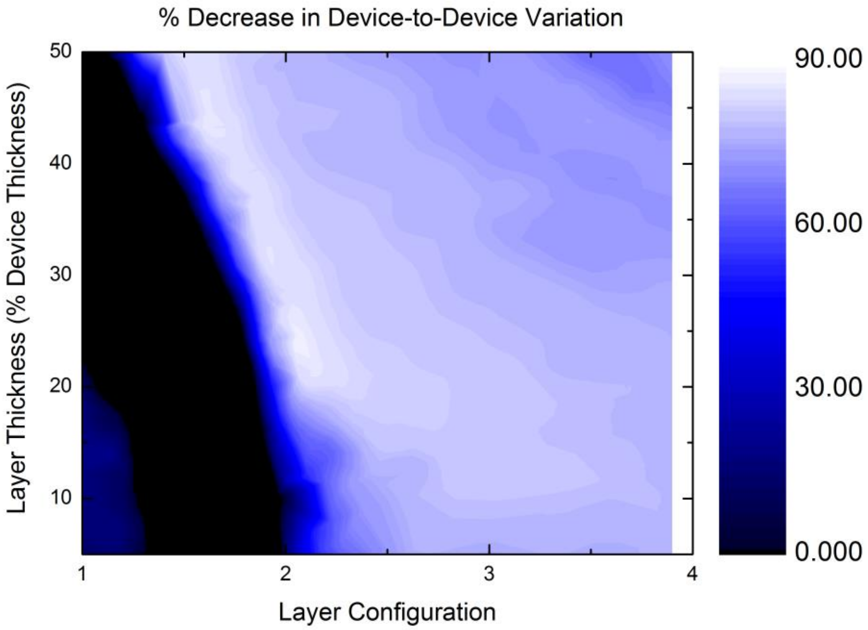

Figure 21: The relative device-to-device (DTD) variability as a function of layer thickness and configuration.

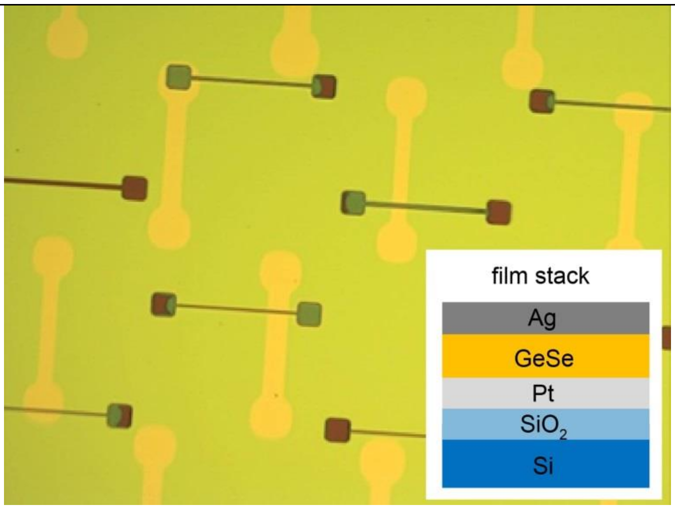
film stack
Ag
GeSe
Pt
SiO_2
Si

Figure 22: Image of GeSeAg resistive memory devices fabricated in MESA

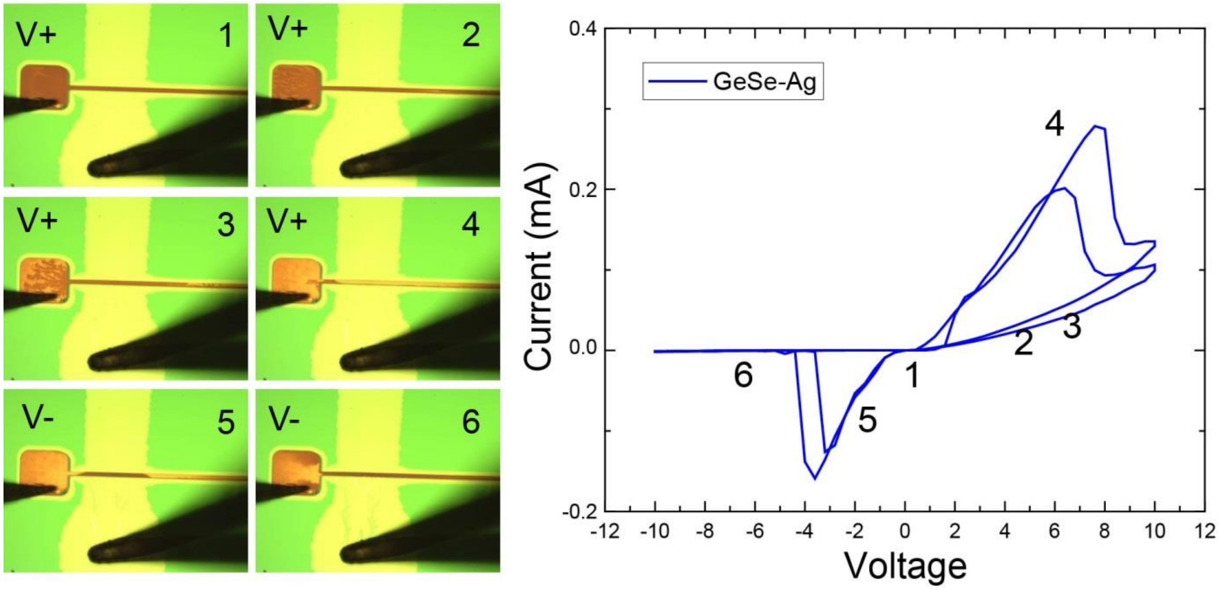

Figure 23: GeSeAg device operation. (left) Upon applying a positive voltage to the top electrode, silver drifts towards the bottom electrode and the device switches on (1-4). Upon applying a negative voltage to the top electrode, silver drifts back to the top electrode and the device switches off (5-6). (right) IV curve of a GeSeAg device with portions of the curve labeled according to the Ag motion shown on the left.

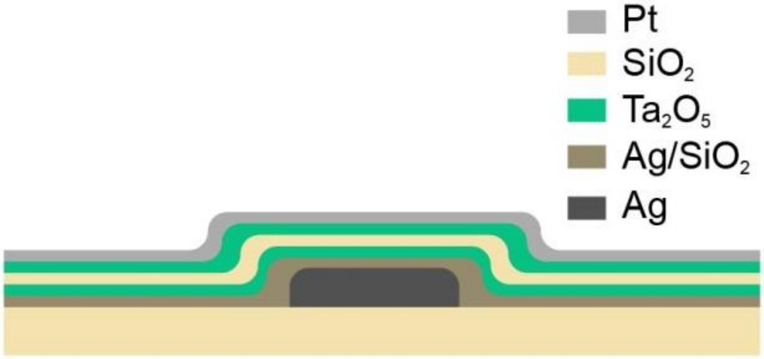
Pt
SiO_2
Ta_2O_5
Ag/SiO_2
Ag

Figure 24: Schematic of a multilayer memristor stack using silver as the electrochemically-active electrode and platinum as the inert electrode.

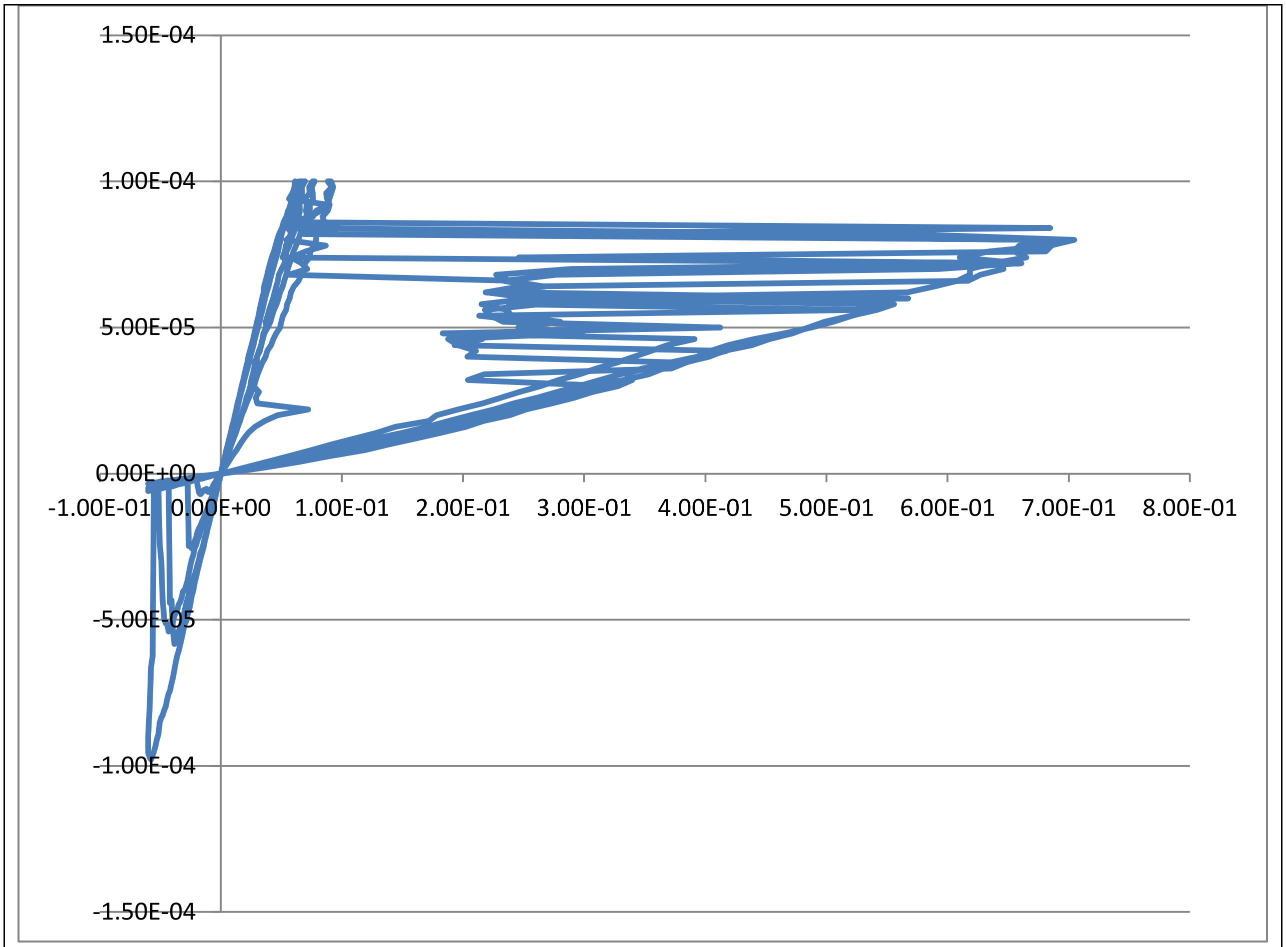

Figure 25: IV switching curve for a single layer (TaOx) resistive memory device with a 20x20 μm^2 active area.

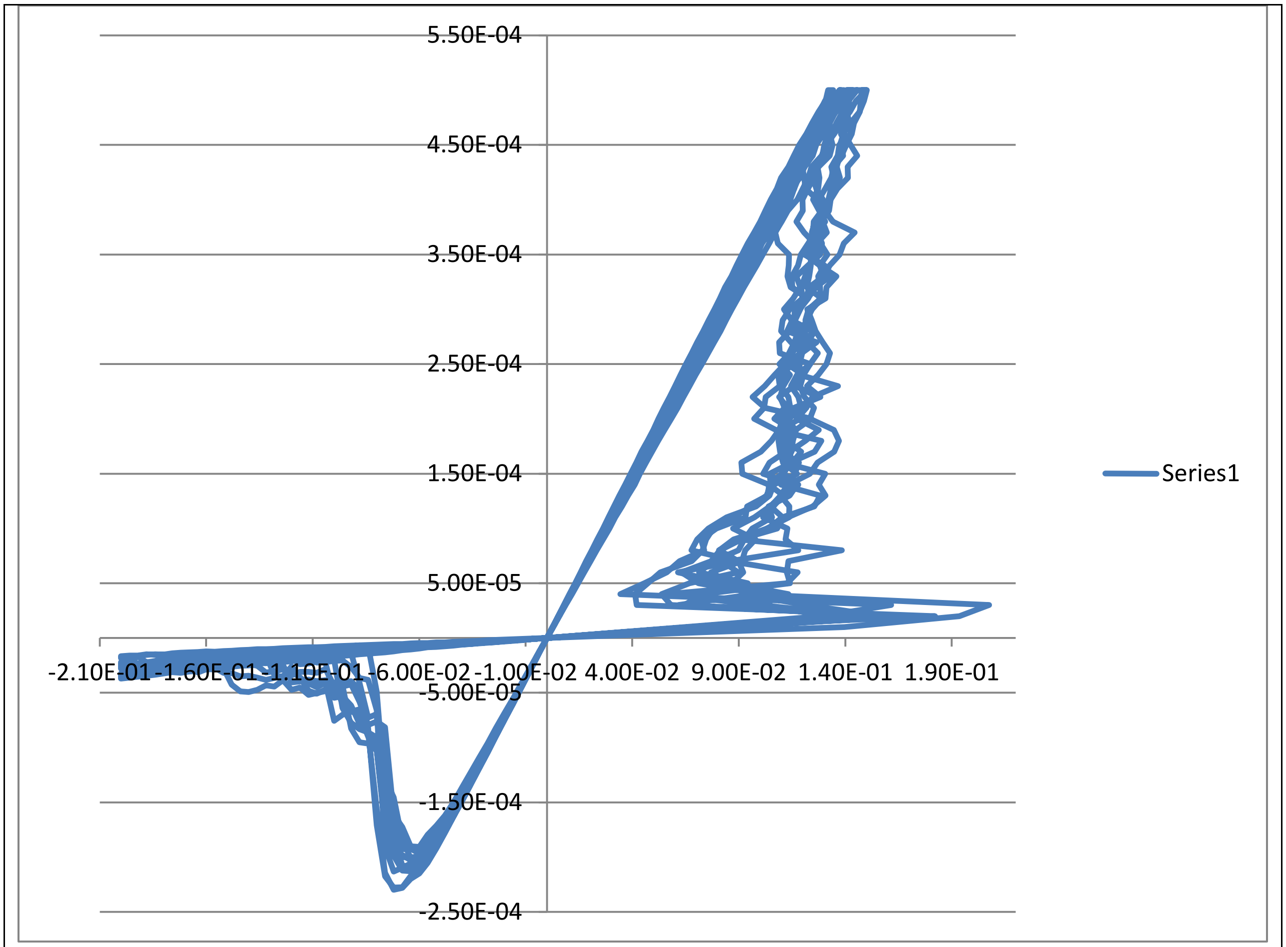

Figure 26: IV switching curve for a single layer (SiO_2) resistive memory device with a 100x100 μm^2 active area.

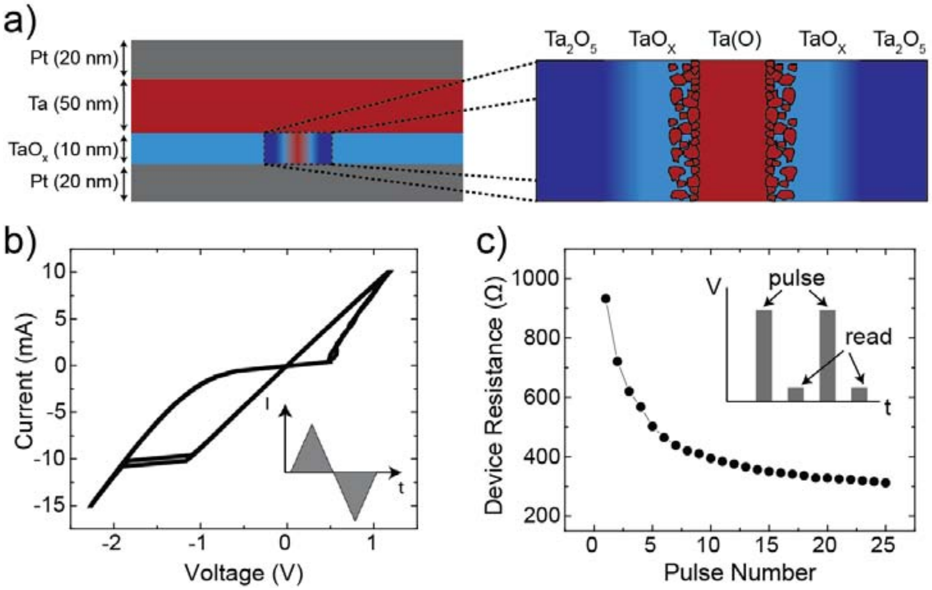

Figure 27: a) Memristor device structure, with the switching region magnified for clarity. b) A hysteretic IV curve from a tantalum oxide device with two stable resistance states (R_{OFF}/R_{ON} > 10). Inset: Triangular current waveform applied in IV hysteresis curves. c) Memristor resistance as a function of pulse number. Inset: The pulse/read waveform sequence used to modulate and measure the device state.

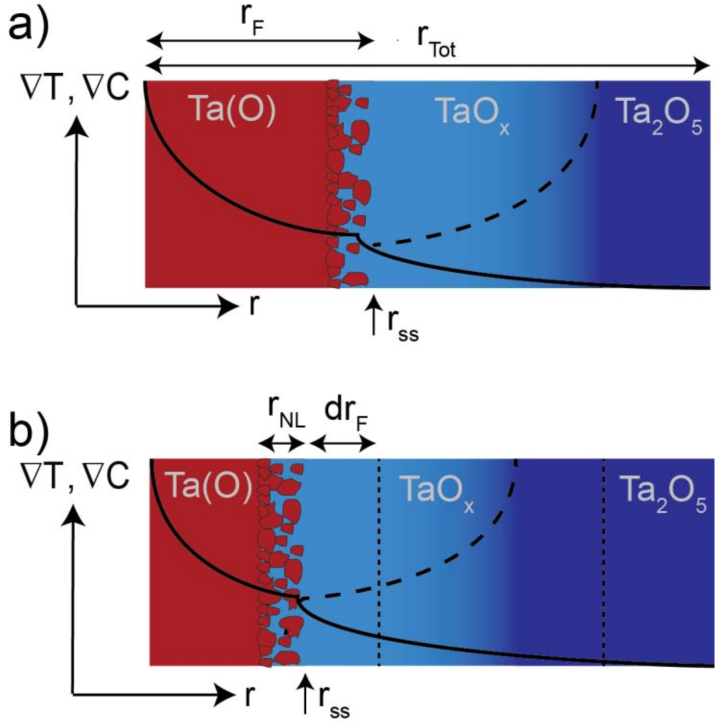

Figure 28:a) The low resistance state geometry of the switching region is shown. A Ta-rich core is surrounded by an oxygen concentration gradient (dashed line), transitioning from a sub-oxide region (TaO_x) to the Ta_2O_5 phase. The steady state filament radius, r_{SS}, is determined by the balance of flux due to the concentration gradient and temperature gradient (solid black line). The discontinuous outer edge contributes to non-linear conduction throughout r_{NL} and causes ruptures as r_F decreases. b) Geometry changes with an increase in resistance are shown: smaller steady-state radius, steeper temperature gradient, and an expansion of the Ta_2O_5 phase and contraction of the Ta filament by the amount dr_F.

Figure 29: a) Device resistance is shown as a function of applied voltage pulse number for ON switching, as calculated from the non-perturbative read measurement (V_{read} = 1mV). Each trace is the time-series of resistive switching for specific amplitudes of the 1 µs, state changing voltage pulse, with the arrow representing the direction of increasing amplitude (0.65 V to 1 V). Fits to Eq. 5 are shown in green. b) Equivalent data for OFF switching for voltages ranging from -1 V to -1.75 V.

Figure 30: IV curves measured at multiple resistance states spaced between R_{ON} and R_{OFF}. Fits according to the parallel conduction model of Eq. 6 are shown in green. Inset: Deviation from linear conduction showing the increasing contribution from parallel discontinuous non-linear conduction as the filament radius decreases.

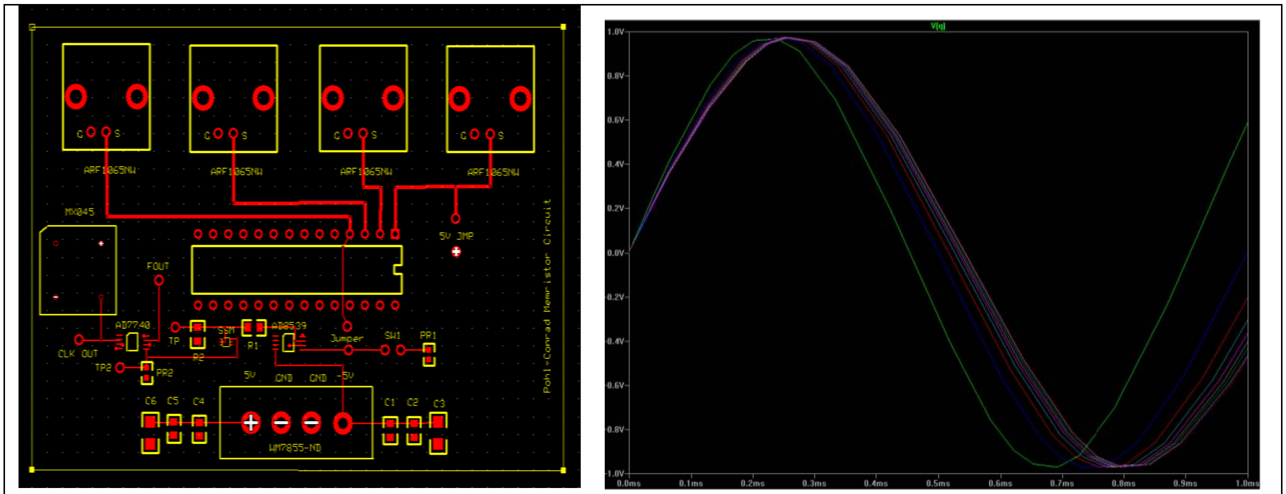
ARF1065NW
ARF1065NW
ARF1065NW
ARF1065NW
G
S
MX045
5V JMP
FOUT
AD7740
TP
SSM
R1
AD8539
Jumper
SW1
PR1
CLK OUT
R2
TP2
PR2
5V
GND
GND
-5V
C6
C5
C4
C1
C2
C3
WM7855-ND
Pohl-Conrad Memristor Circuit
V(q)
1.0V
0.8V
0.6V
0.4V
0.2V
0.0V
-0.2V
-0.4V
-0.6V
-0.8V
-1.0V
0.0ms
0.1ms
0.2ms
0.3ms
0.4ms
0.5ms
0.6ms
0.7ms
0.8ms
0.9ms
1.0ms

Figure 31: (left) Schematic of a voltage to frequency converter circuit using a memristor active element. (right) Spice simulation of the memristor-based voltage to frequency converter.

DISTRIBUTION

1 University of New Mexico
Attn: L. Donald Partridge
MSC08 4740
1 University of New Mexico
Albuquerque, NM 87131-0001

1	MS0886	Patrick Finnegan	1835
1	MS1084	Matthew Marinella	1748
1	MS1084	Andrew Lohn	1748
1	MS1084	Richard Dondero	1748
1	MS1084	Patrick Mickel	1748
1	MS1085	Daryl Dagel	1742
1	MS1085	Olga Spahn	1742
1	MS1085	Steve Wolfley	1747
1	MS1324	Robert Leland	1000
1	MS1327	John Wagner	1462
1	MS1327	Phil Bennett	1463
1	MS1425	Stephen Casalnuovo	1714
1	MS1425	Conrad D. James	1714
1	MS1425	Adrian Schiess	1714
1	MS0899	Technical Library	9536 (electronic copy)
1	MS0359	D. Chavez, LDRD Office	1911
1	MS0161	Legal Technology Transfer Center	11500

Sandia National Laboratories